



**NATIONAL UNIVERSITY OF SCIENCE AND TECHNOLOGY
POLITEHNICA BUCHAREST
DOCTORAL SCHOOL: CHEMICAL ENGINEERING AND BIOTECHNOLOGIES**

Decision no..... date

SUMMARY OF DOCTORAL THESIS

***Transfer de masă la coroziunea terminalelor de
produse petroliere***

Mass transfer in the corrosion of oil terminals

Scientific coordinator: Prof.dr.eng. Tănase DOBRE

Author: Eng. Marius Ciprian ILIE

DOCTORAL COMMITTEE

Chairman	Prof.dr.eng. Pârvulescu Oana	from	NUST Politehnica Bucharest
Scientific coordinator	Prof.dr.eng. Dobre Tănase	from	NUST Politehnica Bucharest
Member	Prof.dr.eng. Lisa Gabriela	from	UST Gh. Asachi Iași
Member	Prof.dr.eng. Chiș Timur	from	UPG Ploiești
Member	Prof.dr.eng. Văireanu Dănuț	from	NUST Politehnica Bucharest

BUCHAREST

2023

Content of thesis summary

1. Introduction	3
2. Content of doctoral thesis	4
3. Structure of doctorat thesis	5
Selective references:	6
CHAPTER 1	7
Selective references:	7
CHAPTER 2	7
Selective references:	8
CHAPTER 3	8
Selective references:	9
CHAPTER 4	9
Selective references:	12
CHAPTER 5	12
Selective references:	31
CHAPTER 6	31
ANNEXES - Supplemental materials for observing the corrosion process in the droplet.....	45
4. Conclusions of thesis	49

1. Introduction

Fossil fuels are a determining part of any economy, with influences that affect practically all fields of activity. Not a single forecast manages to convince that this tendency to continue to use mostly these fuels would vary in intensity, although climate change is not only knocking at the door, but has already crossed the threshold. Large global economies (emerging or developed) put self-interest before global human interest, and the consumption of fossil fuels is huge, which requires huge productions, and this whole roller coaster does not seem to find a brake. If in the field of energy alternative fuels are making up for the gap [1], the same is not happening in the case of petroleum fuels. And this oil/politics/economy/national interest complex is hard to navigate, no matter which side you try. However, an even wider awareness of the consequences of non-adherence to green chemistry can be tried and a more efficient resource management can be tried, both in parallel with the migration to green solutions in addition, for years put, scientifically, on the table by researchers from the field.

We wanted to enter this field of fuel management with this work, namely in the field of safety and security in the oil terminal industry, where studies of some phenomena with direct consequences on the infrastructure of the terminals, would lead to strategies on the prevention side. Corrosion or erosion [2] can still be studied, and the studies in turn can provide applicable solutions.

The effects of corrosion over time can have consequences characterized by a low degree of hazard or, on the contrary, can be associated with the occurrence of leaks, contamination, both of the products and of the environment, or reactions with the materials stored in these tanks and reservoirs.

In this context, we present in this work an extensive investigation, on a laboratory scale, of corrosion in atmospheric conditions, through a study of mass transfer in film corrosion and also of mass transfer in droplet corrosion, followed by the construction of some mathematical models, which properly describe the phenomena, so that these models are used to predict the behavior of structures of the mentioned type, over long periods of time.

Familiarization with the multiple processes and phenomena characteristic of the field of corrosion, through an intensive study of the specific literature, was a first objective of the thesis.

Through our own experimental research, we proposed a second objective of the thesis, namely the construction of two laboratory installations, simultaneously with the elaboration of the work methodology, so that the dynamics of surface corrosion of steel can be characterized when a corrosive environment is in flow film, respectively remains on the surface.

A third objective of the thesis was the development of two mathematical models, respectively their numerical conversion, in order to identify the process parameters, namely: the *apparent constant of the surface corrosion rate*, the *surface oxidation yield* of Fe^{+2} to Fe^{+3} , of the *oxygen diffusion coefficient through the superficial layer of rust*, as functions dependent on the factors influencing the process.

The last proposed objective was to approach *corrosion by evaporation - droplets with NaCl content*, where the involvement of Cl^- ions in the anodic corrosion process is known, respectively to verify that we can use the *evaporation-corrosion model* with the interphase transfer surface variable in time and with transfer and surface chemical reaction, where Cl^- strongly increases the surface reaction rate constant and the oxygen diffusion coefficient, through the rust layer.

The present summary provides a brief presentation of the thesis chapters, detailing sufficiently aspects of chapters 4, 5 and 6, which contain their own elements brought to the problem of mass transfer with chemical reaction on the surface of the solid.

2. Content of doctoral thesis

CHAPTER 1	8
GENERAL/MOTIVTION/OBJECTIVES	8
1.1. MOTIVATIONAL CONTEXT	8
1.2. OBJECTIVES OF DOCTORAL THESIS	9
1.3. STRUCTURE OF DOCTORAL THESIS	9
BIBLIOGRAFIE	11
CHAPTER 2	12
PETROLEUM PRODUCTS TERMINAL - STORAGE SYSTEM - RAW MATERIALS AND PETROLEUM PRODUCTS DISTRIBUTION	12
2.1. PETROLEUM PRODUCTS TERMINAL - GENERAL	12
2.2. OIL TERMINALS IN ROMANIA - PROCESSES AND EQUIPMENT IN OPERATING OIL TERMINALS	15
2.3. INTERNAL AND EXTERNAL CORROSION OF OIL TERMINAL EQUIPMENT	17
2.4. CONCLUSIONS	19
REFERENCES	20
CHAPTER 3	21
ATMOSPHERIC CORROSION OF METAL SURFACES	21
3.1. INTRODUCTION TO ATMOSPHERIC CORROSION	21
3.2. MATHEMATICAL MODELS OF ATMOSPHERIC CORROSION	22
3.2.1. Mathematical models for atmospheric corrosion	23
3.2.1.1. Statistical models	24
3.2.1.1.a. Mathematical functions in deterioration by corrosion	24
3.2.1.1.b. ISO Corrag	24
3.2.1.1.c. The ICP Materials project	25
3.2.1.1.d. The MICAT project	25
3.2.1.1.e. Topographic influences on wind speed in atmospheric corrosion	26
3.2.1.2. Phenomenological models of corrosivity factors	27
3.2.1.2.a. Pollutant mass transfer for a (metallic) surface	27
3.2.1.2.b. Maritime transport of aerosols	27
3.2.1.2.c. Sub-droplet corrosion	28
3.2.1.2.d. Wind speed factor	29
3.2.1.3. Atmospheric corrosion maps	29
3.3 CONCLUSIONS	30
REFERENCES	30
CHAPTER 4	33
CORROSION, PICKLING AND ETCHING OF METAL SURFACES	33
4.1. CORROSION, PICKLING AND ETCHING: SIMILARITY AND DIFFERENCE	33
4.2. PICKLING METHODS	34
4.3. INTRODUCTION TO CORROSION AS A CHEMICAL SURFACE PROCESS. SIMPLE MODELS	35
4.4. SIMPLE MODELS FOR PICKLING. THE INFLUENCE OF FACTORS ON PROCESS KINETICS	38
4.4.1. Mathematical models in cases of metal pickling	38
4.4.1.1 Introduction	38
4.4.1.2 Method and experimental investigation	39
4.4.1.3 Results and discussion	42
4.4.1.4 Conclusions	44
REFERENCES	44

CHAPTER 5	46
FILM FLOW AND CORROSION OF OIL TERMINALS	46
5.1. DESCRIPTIVE ELEMENTS, RAIN - ITS INTENSITY AND FREQUENCY	46
5.2. EXPERIMENTAL INSTALLATION, OBJECTIVES, EXPERIMENTAL DATA IN THE INVESTIGATION OF FILM FLOW CORROSION	49
5.2.1. Experimental data and research stages	52
5.3. MATHEMATICAL MODEL FOR THE COUPLING OF MASS TRANSFER AND SURFACE REACTION IN FILM FLOW CORROSION	60
5.3.1. Introduction	60
5.3.2. Materials and procedure	64
5.3.2.1. Experimental installation and method	64
5.3.2.2. Mathematical modeling	67
5.3.2.3 Results	75
5.3.2.4. Discussions	81
5. Conclusions	85
REFERENCES	85
CHAPTER 6	88
DROPLET CORROSION AT PETROLEUM PRODUCTS TERMINALS	88
6.1. WET AIR AND DEW DROP FORMATION	88
6.2. MASS AND HEAT TRANSFER CONSIDERATIONS DURING DROPLET FORMATION	91
6.3. EXPERIMENTAL INVESTIGATION OF MULTIPLE DROPLET CORROSION ON PLATE	95
6.3.1. Introduction	95
6.3.2. Experimental installation and method	97
6.3.3. Mathematical modeling	100
6.3.4. Results	106
6.3.5. Discussions	110
6.3.6. Conclusions	116
REFERENCES	117
ANEXE - Supplemental materials for observing the corrosion process in the droplet	121
CHAPTER 7	126
GENERAL CONCLUSIONS	126

3. Structure of doctorat thesis

For this paper, it was decided that the structure of the chapters should be similar to that of the scientific journals in which the results of the experimental research were disseminated, for two reasons: i) because this approach allows easy tracking of the achievement of the proposed objectives, the experimental technique used, the hypotheses the models and subsequently their course, the description of the results obtained and the associated discussions; ii) because we show that the experimental research, or rather the research results were presented exactly on the model of their publication after acceptance in the specialized journals.

It would be expected that the volume of data existing in the corrosion literature would allow one to state that everything is in place and that everything is under control. However, the field of corrosion is characterized by great complexity and current situations that demonstrate, regularly, that the presence expressed through corrosion control cannot still be stuck in the area where an incident (not to say disaster) just happened, precisely because of this. The multiple types of corrosion, the factors and parameters that must be taken into account when these corrosion phenomena occur, the type of (property) transfer, the mechanisms through which they occur, the possible combination of two phenomena in the same process, all these are, in addition to challenges, and the space where not being totally under control, we can *approach* corrosion with solutions associated with mathematical models.

The doctoral thesis begins with the presentation in Ch. 1, in short, of the motivational context and the objectives proposed for the doctoral research, respectively with the summary of the thesis by chapters.

In Ch. 2 we begin the oil terminal study, with generalities in the first part and with a presentation in subchapter 2.2 of the petroleum product terminals owned by companies in Romania, as well as with the description of specific equipment for carrying out activities in these petroleum product terminals. Subchapter 2.3 introduces us to the field of corrosion and, in particular, of internal and external corrosion, specific to petroleum product terminals, also with generalities, briefly.

With Ch. 3 we enter the area of atmospheric corrosion literature study, with an *Introduction* and some definitions, after which we present in subchapter 3.2 *Mathematical models for atmospheric corrosion*. Being an extremely complex field, we managed to find literature data that in turn helped us to show in an orderly, somewhat chronological way, how the atmospheric corrosion of metal surfaces should be approached, the risk factors, some variables that we had not taken into account calculation and, obviously, some solutions, not necessarily for prevention, but especially for future approaches in experimental research. However, both subchapter 3.2.1 and subchapter 3.2.2 lead the study to a conclusion regarding the main requirement, that of benefiting from a corrosion map, i.e. either having it or building it and without that you cannot address a minimum number of steps in corrosion investigation.

In Ch. 4 corrosion, pickling etching were addressed, as phenomena of transport and chemical reaction on a metal surface, with a parallel between them and some of the characteristics of these processes, in terms of causes and stages. In subsection 4.2 models have been described that characterize the vast majority of corrosion processes that take place on the metal surface (of equipment in the oil industry in our case), so we were able to state that, in these cases, corrosion is a surface chemical process..

With subchapter 4.3 we start the experimental part of this work, where the experimental study on the pickling process of metallic surfaces, with the kinetics of the process and with the development of a mathematical model, was presented.

Ch. 5 presents the study of film corrosion, extremely present in the case of oil product terminals and tank farms, but not only. Theoretical notions about film corrosion can be found in subchapter 5.1, and subchapter 5.2 presented the experimental investigation and insisted on the presentation of the experimental procedure (subsequently addressed in subchapter 5.3), with a detailed description of the construction of the experimental facility, with the proposed strategy for data collection (what type of data, the method of obtaining, the method of processing), as well as with the presentation of the progress characteristic of the stages of experimental research. Being a relatively large volume of data and information, it was preferred to present them in this subchapter, so that it could be possible for subchapter 5.3 to present the results and discussions of the investigation on the model of disseminating them in the specialized journal in which it was published.

Ch. 6 is almost identical in structure to Ch. 5, but here droplet corrosion was investigated. A study of vapor condensation and droplet formation was introduced in subchapter 6.1, to facilitate the experimental investigation presented later. In subchapter 6.2, the procedure was similar to that in subchapter 5.2, namely with the highlighting of the experimental procedure, the proposed strategies and the progress during the research, so that in subchapter 6.3 the results and discussions of the investigation are presented in the same way, on the model of disseminating them in the scientific journal in which it was published.

Ch. 7 was dedicated to the general conclusions, resumed as a recapitulation of the partial ones, because each chapter had its own bibliography and its own conclusions.

Selective references:

1. <https://economedia.ro/productia-europei-de-energie-electrica-din-eoliene-si-solar-a-depasit-o-pentru-primadata-pe-cea-din-gaz.html>
2. Frayne, C. Environmental Modification for Cooling, Heating and Potable Water Systems. *Shreir s Corrosion*, 2010, 2930–2970, doi:10.1016/b978-044452787-5.00161-x

4. Summary of doctoral thesis

CHAPTER 1

Chapter 1 includes a brief presentation of the motivational context, where it is emphasized that the effects of corrosion over time, which can have consequences characterized by an important degree of hazard or the occurrence of leaks, contamination, both of the products and of the environment, can constitute a motivating impulse for the experimental study of this complex process, which would lead to the development of prevention, safety and security strategies in the oil terminal industry. It then continues with the objectives proposed in this experimental doctoral research, so that at the end of the chapter we find the summary of the thesis (structure by chapters).

Selective references:

3. <https://economedia.ro/productia-europei-de-energie-electrica-din-eoliene-si-solar-a-deposit-o-pentru-primadata-pe-cea-din-gaz.html>
4. Frayne, C. Environmental Modification for Cooling, Heating and Potable Water Systems. *Shreir s Corrosion*, **2010**, 2930–2970, doi:10.1016/b978-044452787-5.00161-x

CHAPTER 2

In Chapter 2, we entered the oil terminal study field, with generalities and the presentation of oil terminals in Romania and an introduction to the field of corrosion. We thus see, at the level of 2023, a distribution, among four companies, of the terminal/pre-treatment and storage infrastructure for petroleum products, regardless of whether they have access by sea or only by road/railway. Infrastructure sectors with associated equipment, with potential exposure to the phenomenon of erosion-corrosion, were also listed in order to understand the size of the field in which the study can be entered. Although corrosion is relatively difficult to classify in a successful simplification, it was presented at the end of the chapter to group it into *internal corrosion* (Table 2.2. in the thesis), *external corrosion* (with a general definition presented), respectively *galvanic corrosion*, which is a combination of the first two.

Table 2. 1 Types of corrosion to which the equipment of a petroleum products terminal can be exposed [11]

Nr.crt.	Denumire	Causative factors	Characteristics
1	Corrosion-erosion	Fluid velocity, turbulent flow, sudden pressure drop	Combination of the two phenomena
2	Corrosion fatigue	Frequent application of pressure or mechanical forces	It can be of: initiation, propagation and final
3	Fretting Corrosion	Metal-on-metal friction/sliding	Prevention may include the use of hard materials, or lubrication
4	Microbial corrosion	Microorganisms, biological agents	It occurs through the biological formation of hydrogen sulfide
5	CO ₂ Corrosion	CO ₂ , secondary product from crude oil and gas	Acidic properties on contact with water
6	H ₂ S Corrosion	H ₂ S secondary product from crude oil and gas	Acidic properties on contact with water. Generators of 4 other distinct types of corrosion: 1. Corrosion by stress cracking; 2. Hydrogen-induced cracking; 3. Corrosion by stress cracking with sulphides; 4. Step cracking

7	Crevice Corrosion	Metal/metal contact, sealing areas with imperfections	It takes place in the area of cracks
8	Cavity corrosion	Sea water, <i>Cl</i>	Hard to predict
9	Stress corrosion cracking	Combination of stress and corrosive compounds	Creation and expansion of cracks
10	Intergranular Stress Corrosion Cracking	Carbide migration and chromium carbide formation	Prevention: use of austenitic stainless steels
11	Corrosion under insulation	Fluid access between insulation and metal	Care in making the insulation

Selective references:

1. <https://energyindustryreview.com/oil-gas/omv-petrom-completed-the-modernization-of-the-fuels-terminal-in-arad/>
2. <https://www.oiltanking.com/en/news-info/glossary/tank-storage-tank-terminals.html>
3. Al-Moubaraki, A.H.; Obot, I.B. Corrosion challenges in petroleum refinery operations: Sources, mechanisms, mitigation, and outlook, *Journal of Saudi Chemical Society*, **2021**, *25*, 101370.
4. Speight, J.G. High acid crudes. *Gulf Professional Publishing*, **2014**, <https://doi.org/10.1016/C2013-018868-X>
5. <https://www.rompetrol.com/ro/proiecte-si-investitii-majore/midia-marine-terminal>
6. <https://lukoil.ro/ro/ForBusiness/SalesofPetroleumProducts>
7. Sotoodeh, K. Subsea Valves and Actuators for the Oil and Gas Industry. *Gulf Professional Publishing*, **2021** <https://doi.org/10.1016/B978-0-323-90605-0.00006-2>, ISBN: 978-0-323-90605-0
8. Roberge P.R. Handbook of Corrosion Engineering, Th. Edition, *McGraw-Hill*, **2019**, ISBN: 978-1-26-011696-0

CHAPTER 3

Chapter 3 presents the theoretical study of some aspects of atmospheric corrosion, which, in addition to the laboratory experimental set up (objective 2), introduces the third objective of the research, namely the development of a new type of mathematical models associated with corrosion. The theoretical study showed the need to identify the elementary factors and processes that determine atmospheric corrosion, including the mathematical models developed for this category of corrosion. It should be noted that, concretely, atmospheric corrosion refers specifically to the situation of exposure of a surface (metallic in our case) to environmental conditions with water and oxygen as the limiting reactant, without an express reference to a particular form or type of corrosion.

We thus note that the factors with the greatest influence in atmospheric corrosion are, by far, humidity, in all its forms (rain, dew, condensation) [1] together with oxygen. In the absence of moisture, most contaminants would have little or no corrosive effect. A fundamental condition for atmospheric corrosion processes is the presence of a thin-film electrolytic film that can form on the metal surface when these surfaces are exposed to a critical level of humidity. Even if this film is almost invisible, the corrosive contaminants inside this film can reach relatively high concentrations, under alternating wetting and drying conditions. Atmospheric corrosion is thus initiated, in the presence of this film, through an anodic and cathodic reaction (Equations 1 and 2) [1].



A large number of factors influence the rate of corrosion, most importantly the frequency and intensity of rainfall and the condensation and evaporation of water on the corrosion surface. A number of ten mathematical models were presented in this chapter and aspects regarding the characteristic phenomenological methods were detailed, highlighting the role of the factors on the transport and transfer to the corrosion surface, of the active (O_2) and activating (Cl^- , SO_4^{2-} etc.) in the process.

Selective references:

1. Winston, R. R. Uhlig's Corrosion Handbook, Third Edition, John Wiley & Sons, **2011**, ISBN 978-0-470-08032-0
2. Knotkova, D. 2005 F. N. Speller Award Lecture: Atmospheric Corrosion—Research, Testing, and Standardization, *Corrosion*, **2005**, 61, 723–738.
3. Leygraf, C.; Graedel, T.E. Atmospheric Corrosion, Wiley, New York, **2000**
4. Steinmayer, R.F. Land Vehicle Management. AGARD Lecture Series No. 141, NATO, Neuilly-sur-Seine, France, **1985**.
5. Hou, W.; Liang, C. Eight-Year Atmospheric Corrosion Exposure of Steels in China. *Corrosion*, **1999**, 55, 65–73.
6. Morcillo, M.; Almeida, E.; Marrocos, M.; Rosales, B. Atmospheric Corrosion of Copper in Ibero-America. *Corrosion* **2001**, 57, 967–980.
7. The Zinc Millennium Map Provides Potential Cost Savings, Anti-Corros. Methods Mater., **2001**, 48, 388–394.

CHAPTER 4

In chapter 4, corrosion, pickling and etching were addressed, as phenomena of transport and chemical reaction on a metal surface, initially introductory, in subchapters 4.1 - 4.3. Regarding the similarity and differentiation between corrosion, pickling and etching, we find that the first common characteristic of the three phenomena is that they occur through the action applied to the surface of the materials (in our case metallic), more precisely as a result of a surface reaction. Corrosion (internal and external) was explained in chapter 2 and we note that it is an undesirable phenomenon (but which occurs anyway, when the conditions are met) in a specific environment (atmospheric or marine). On the other hand, however, the other two processes are voluntary, which come to repair or prevent (in most cases) the consequences of corrosion. And in this chapter, four mathematical models associated with the described processes were presented, the first three being from the literature, and the fourth being developed and supported by our experimental study, presented in subchapter 4.4. Here, on the model of scientific journals, the experimental results (published in the Bulletin of Romanian Chemical Engineering Society, 2020) were presented in cases of metal pickling and, in particular, copper pickling by immersion in ammonium persulfate/sulfuric acid solutions, used to customize the kinetics of this process, by simultaneously solving the species flow and diffusion equations. It was thus stated that for immersion pickling, the basic phenomena take place inside the boundary layer of natural convection, formed on the surface of the metal part. In this situation, a mathematical model can be developed by simultaneously solving the flow and species diffusion equations [23]. At the surface of the pickling material, the chemical reaction that characterizes the process generates species A, which becomes responsible for the kinetic evolution of the pickling. Figure 4.1 shows the development of the boundary layer at the pickling surface and that the transfer flux of species A evolves here. If a quasi-stationary evolution of pickling is considered, then the mathematical model of the process is given by the system of Equations (1), which contains the flow equation imposed by the concentration gradient ($c-c_\infty$) and the species diffusion equation, which has the concentration c_p to the pickling surface. To be active, the mathematical model requires the conditions of univocity. At given y , these conditions are expressed by Equation (2) and Equation (3).

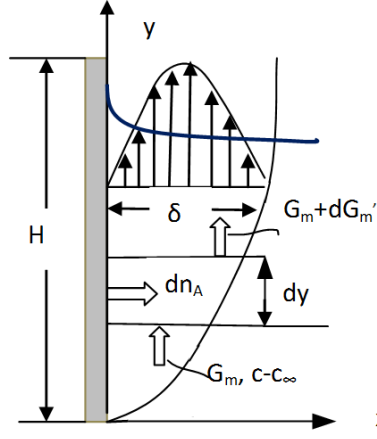


Figure 4.1. Phenomenological surface processes in pickling by immersion in solutions

$$\begin{cases} \nu \frac{\partial^2 w_y}{\partial x^2} + g\beta_c (c - c_\infty) = 0 \\ w_y \frac{\partial c}{\partial y} = D \frac{\partial^2 c}{\partial x^2} \end{cases} \quad (1)$$

$$x = 0, \quad c = c_p, \quad w_y = 0 \quad (2)$$

$$x = \delta, \quad c = c_\infty, \quad \left(\frac{\partial c}{\partial x} = 0 \right), \quad w_y = 0 \quad (3)$$

A simplified method can be used to solve the model analytically. In this sense, it is considered that the dimensionless concentration profile of the diffusible species, inside the boundary layer at the pickling surface, depends only on x and follows Equation (4). The conditions for c in Equation (2) and (3) particularize the dimensionless concentration of the diffusible species in Equation (5). From the expression of the definition of the mass transfer coefficient of the species (6) it is observed that the solution of the flow equation must produce a relation for the thickness of the boundary layer, δ .

$$\Gamma_A = \frac{c - c_\infty}{c_p - c_\infty} = a + bx + cx^2 \quad (4)$$

$$\Gamma_A = \left(1 - \frac{x}{\delta} \right)^2 \quad (5)$$

$$k = \frac{-D \frac{dc}{dx} \Big|_{x=0}}{c_p - c_\infty} = -D \frac{\partial \Gamma_A}{\partial x} \Big|_{x=0} = \frac{2D}{\delta} \quad (6)$$

After solving the flow equation for the pickling model, the expression of the mean flow rate was obtained, given by Equation (13).

$$\bar{w}_y = \frac{1}{\delta} \int_0^\delta w_y dx = \frac{A\delta^2}{40} = \frac{g\beta_c \delta^2}{40\nu} (c_p - c_\infty) \quad (13)$$

The balance of species A, relative to the control volume in Figure 1, which have unit height and width dy , goes to Equation (14). Considering the mass flow per unit width of the wetted surface (Equation 15), Equation (14) becomes Equation (16) (in the thesis). With $\delta = 0$ at $y = 0$ from (16), the local values of the mass transfer coefficient and its mean value are successively obtained (Equation (17) and Equation (18) respectively).

$$k = \frac{2D}{\delta} = 0,74 \left(\frac{gD^3 \beta_c (c_p - c_\infty)}{\nu y} \right)^{0,25} \quad (17)$$

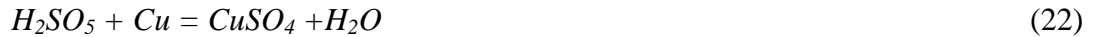
$$k = \frac{1}{H} \int_0^H k dy = 0,99 \left(\frac{gD^3 \beta_c (c_p - c_\infty)}{\nu H} \right)^{0,25} \quad (18)$$

$$N_p = c \left(\frac{D^3}{\nu H} \right)^{0,25} c_{pa}^{1,25} \quad (19)$$

To validate the presented model, the experimental investigation of copper pickling using acidic solutions of ammonium persulfate was developed. An experimental design 2³, where the process factors are temperature, ammonium persulfate concentration and sulfuric acid concentration in the pickling solution, respectively, was selected for data collection. The copper samples with 10 cm length (H = 0.1 m) and 2 cm width, were immersed, with a vertical position for a determined time, in 1.5 L of pickling solution. The pickling flux was calculated, from experimental data, with Equation (20), where $m_\tau - m_{\tau+\Delta\tau}$ represents the mass of dissolved (pickled) copper in the time period $\Delta\tau$ between two successive measurements

$$N_{Cu,ex} = \frac{m_\tau - m_{\tau+\Delta\tau}}{S\Delta\tau} \quad (20)$$

The chemical reactions occurring at the copper pickling surface, when acid persulfate solution is used as a pickling medium, are given by Equations (21) - (22). The presence of sulfuric acid in pickling media prevents the decomposition of Caro acid, so that it is only active for the reaction with copper.



It is noted that copper sulfate is the species whose diffusion controls the pickling flux. From the literature we note that the diffusion coefficient for the Cu^{+2} ion (as the $CuSO_4$ diffusion coefficient), in 0.1 M $CuSO_4$ /0.2-0.8 M H_2SO_4 electrolyte, was found to be $5.23 \cdot 10^{-10}$ m²/sec, at 25 °C. And this value was accepted for use in our model. For each pickling solution, the viscosity was determined experimentally. Table 1 contains the experimental conditions and the measured pickling flux. In the same table we have included the measured kinematic viscosity of the pickling solutions and the diffusion coefficient of copper sulfate obtained by temperature correction of the value mentioned above. The last column of Table 4.1 contains the calculated values for the constant c of Equation (19).

Table 4.1 Experimental pickling flow and calculated values for c from Eq. (19)

Nc	t °C	c_{aps} g/l	c_{as} g/l	$N_{Cu,ex}$ kg/m ² s	ν m ² /s	D m ² /s	c Ec. (19)
1	40	150	15	$2.075 \cdot 10^{-4}$	$6.79 \cdot 10^{-7}$	$7.66 \cdot 10^{-10}$	0.039
2	40	150	7.5	$1.813 \cdot 10^{-4}$	$6.69 \cdot 10^{-7}$	$7.81 \cdot 10^{-10}$	0.035
3	40	75	15	$1.196 \cdot 10^{-4}$	$6.61 \cdot 10^{-7}$	$7.88 \cdot 10^{-10}$	0.045
4	40	75	7.5	$1.031 \cdot 10^{-4}$	$6.59 \cdot 10^{-7}$	$8.02 \cdot 10^{-10}$	0.043
5	20	150	15	$9.852 \cdot 10^{-5}$	$1.13 \cdot 10^{-6}$	$5.05 \cdot 10^{-10}$	0.029
6	20	150	7.5	$9.689 \cdot 10^{-5}$	$1.11 \cdot 10^{-6}$	$5.11 \cdot 10^{-10}$	0.029
7	20	75	15	$6.438 \cdot 10^{-5}$	$1.08 \cdot 10^{-6}$	$5.22 \cdot 10^{-10}$	0.039
8	20	75	7.5	$5.998 \cdot 10^{-5}$	$1.04 \cdot 10^{-6}$	$5.29 \cdot 10^{-10}$	0.039
9	30	112	11.2	$8.167 \cdot 10^{-5}$	$8.07 \cdot 10^{-7}$	$6.51 \cdot 10^{-10}$	0.026
10	30	112	11.2	$7.987 \cdot 10^{-5}$	$8.07 \cdot 10^{-7}$	$6.51 \cdot 10^{-10}$	0.025
11	30	112	11.2	$8.453 \cdot 10^{-5}$	$8.07 \cdot 10^{-7}$	$6.51 \cdot 10^{-10}$	0.027

It is specified that when calculating the c values, it was considered that the concentration level of active species in the pickling solution c_{pa} is the sum of the concentrations of ammonium

persulfate (c_{aps}) and sulfuric acid (c_{as}). The mean value of the constant c in Equation (19) is 0.035, while their standard deviation is 0.0007.

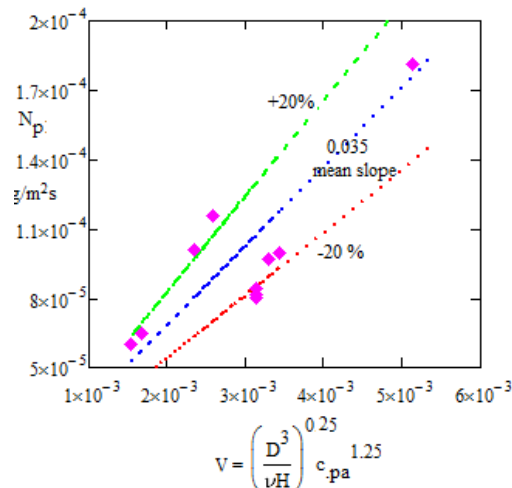


Figure 4.2 Flux dependence of copper pickling vs $\left(\frac{D^3}{\nu H} \right)^{0.25} c_{pa}^{1.25}$

Figure 4.2 shows the evolution of the copper pickling flow as a function of the characteristic term in Eq. (19). We find here that the best value of the constant c in this relationship is 0.035. At the same time, this figure considered a comparison between the experimental values of the pickling flux and those according to the model with $c = 0.035$. With an approximation of $\pm 20\%$ we find that the model has an acceptable response to the experimental data.

Selective references:

1. Bahadori, A. Essentials of Coating, Painting, and Lining. Chapter 1 2015, Pages 1-105 <http://dx.doi.org/10.1016/B978-0-12-801407-3.00001-8>
2. Eun, J-C. T. Handbook of Engineering Practice of Materials and Corrosion, Springer Nature Switzerland AG, **2020**, ISBN 978-3-030-36429-8, <https://doi.org/10.1007/978-3-030-36430-4>
3. Vanaei, H.R.; Eslami, A.; Egbewande A. A review on pipeline corrosion, in-line inspection (ILI), and corrosion growth rate models, *International Journal of Pressure Vessels and Piping*, **2017**, 149, 43-54.
4. Bing T.; Wen, Su.; Jiang,W.; Fenglian, F.; Guojun ,Y.; Jianyan, Z. Minimizing the creation of spent pickling liquors in a pickling process with high concentration hydrochloric acid solutions: Mechanism and evaluation method, *Journal of Environmental Management*, **2012**, 98, 147-154.
5. Dobre T., Floarea O., Engineering Elements of Chemical Surfaces Processing, Chapter 3, Matrix Rom, Bucharest, **1998**
6. Milora, C.; Henrickson, F.G.; Hahn, C.W. Diffusion Coefficients and Kinetic Parameters in Copper Sulfate Electrolytes and in Copper Fluoborate Electrolytes Containing Organic Addition Agents, *J. Electrochem. Soc.: Electrochem. Sci. and Techn.*, **1973**, 120, 4, 488-492.

CHAPTER 5

In chapter 5, film flow and film flow corrosion are investigated, with brief generalities in subchapter 5.1, so that in subchapter 5.2 a detailed description of the experimental set up is presented, with the proposed strategy for data collection (what type of data, how of obtaining, processing method), as well as the progress characteristic of the experimental research stages, where it is shown that for the simulation of complex atmospheric conditions, the supply, on the selected material section, with distilled water, conductivity of $\sigma_{AD}=105 \mu\text{S}/\text{cm}$ was taken into account (where AD = distilled water) continuously, similar to how those in nature are exposed. The goal was to create a continuous film of water, similar to the one created in precipitation conditions, of duration and intensity close to the atmospheric ones.

The study followed the influence of the factors on the corrosion dynamics only on one side of the sheet metal section with the surface $A_T=15 \times 100 = 1500 \text{ cm}^2 = 0.15 \text{ m}^2$. For the protection of the other part of the sheet metal section, it was opted for the chemical treatment with universal enamel and its gluing on the plexiglass support (2), $g_{PL}^1=0.2\text{cm}$ thickness, $L_{PL}=103\text{cm}$ length and respectively $l_{PL}=22\text{cm}$ width. As can be seen from the presentation figure, two PVC supports (3) of $L_{S\text{PVC}}=105 \text{ cm}$ length and $l_{S\text{PVC}}=7 \text{ cm}$ width were attached to the ST/PL joint body on the sides. The black sheet section was thus maintained in a vertical plane with the help of the two PVC supports. Regarding the water supply, the flow on the flat vertical steel plate, this was achieved with the help of two flexible pipes (4) of $D_{C1\text{AD}}^2=D_{C2\text{AD}}^3=1 \text{ cm}$ diameter and $L_{c1}=L_{c2}=150 \text{ cm}$ length, provided at heads with glass nozzles (5). The two pipes are supported by mobile arms (6), attached in turn to two stands (7).

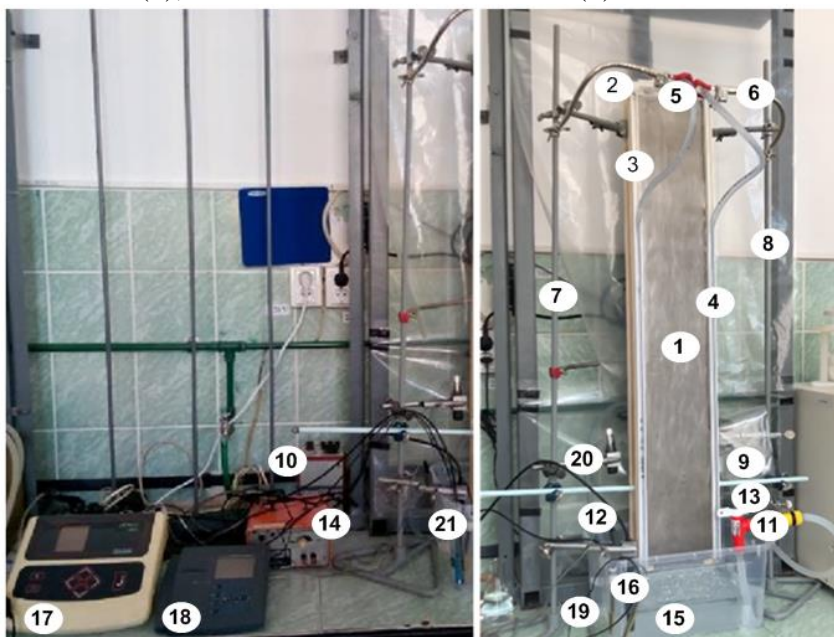


Figure 5. 1 Scheme of the experimental laboratory installation

The water flows feeding the flow in the film can have different values, here considering working with $Gv_{IAD} = 0.4 \text{ L/min}$, $Gv_{IIAD} = 0.9 \text{ L/min}$ respectively $Gv_{IIIAD} = 1.9 \text{ L/min}$. In each case of flow, a uniform film was created, formed on the entire study surface of the section of black sheet steel, on which the simulation of corrosion in the film, as it is formed from precipitation in the natural environment, is considered. Regarding the testing durations by the flow of flows mentioned on the sheet section, values between 180 and 360 minutes were considered ($T_{op\ 1.5\ GvI} = 180\text{-}360 \text{ min}$) for an extended period of time ($T_{op/day}$) (operating time per day) between 24 and 72 hours). The continuous supply of water to the black sheet section was carried out with the help of a pump (9), fed with electric current by a transformer (10), fed in turn at 220 V. The operation at the selected flow rates was carried out using a control valve (11), mounted at the suction of the pump (peristaltic pump). The supply to the two pipes, with flow rates of equal values, was achieved by mounting a 50 cm pipe at the pump outlet to which the splitter (12) was attached. In order for there to be a homogeneous medium (perfect mixing) in the recirculation vessel, as well as to achieve good aeration (oxygenation) of the recirculated water, it was realized continuous mixing with a laboratory stirring system composed of motor (13) fed with an alternating current, with stirring device and electrical feeding system with voltage regulation Agituar (14). Supplying the continuous film with distilled water over the entire width and length of the entire steel sheet section was achieved by recirculating, from the supply vessel (15), with the help of the pump, the entire volume of distilled water. The volume of water in the

¹ PL= plexiglass

² DCAD = distilled water pipe diameter

³ DCAD = distilled water pipe diameter

vessel was fixed at the value $V_{AD}=5$ L. As shown in the feeding vessel, the accumulation of Fe ions takes place that do not participate in the local formation (at the site of the corrosion pile) of the rust accumulation. This accumulation of ions in the recirculated water can be followed conductometrically and by spectrophotometric analysis. Therefore, 2 conductivity sensors were mounted in the supply vessel, in permanent contact with the recirculated water, one of them (16) connected to a Jenway 330 conductometer (17) and a second one (18) connected to an INOLAB conductometer WTW (19). The Jenway conductometer also has a coupled sensor for temperature measurement (20). In order to know the temperature and humidity of the external air, an additional air humidity, air temperature and air dew point sensor (22) was added to the installation. Thus, during the exposure of the tin plate to the continuous supply of distilled water, measurements were made at intervals of 15 min (Tab. 2.2) of the conductivity, the temperature of the external environment, the temperature of the water, the temperature and the dew point temperature of the air. At time intervals of 60 min, 15 mL of the water sample was taken from the recirculation basin, so that here the concentration of total Fe in the corrosion environment was determined.

The experiments were carried out on cycles of several days, considering as a parameter the modification of the feed rates on the sheet metal surface as well as the possibility of choosing the effective operating times for corrosion by flow in the film. It should be added that, although it was not specified, the simulation of corrosion in film flow through acid rain is easily achieved by controlling the composition of the water in the recirculation tank. An example of data collection can be found in Tab. 5.3.

Tab. 5. 3 Values of the process parameters at the beginning of the first experiment

Feeding flow $Gv_{IAD} = 1.9$ L/min									
Crt. no.	Measure ment range [min]	Sample collection interval [min]	Sampl e no.	Operating time	Pres. atm [mm/Hg]	Mediu m temp [C]	Water temp [C]	Elec. Cond. [μ S/cm]	Ions content [mV]
Day I									
0	0	n/a	n/a	[min]	758.31	27.7	27.9	105.4	415

The state of the sheet metal surface at the initiation of the corrosion process by film flow can be seen in Figure 5.4. The unaltered appearance of the sheet metal surface is observed when the process starts with demineralized water with the electrical conductivity value of $\sigma_{AD0GvI}=105$ μ S/cm (in the Inolab conductometer) respectively of $\sigma_{AD0GvI}=415$ mV (in the Jenway ionometer) at $t_{med atm}= 27.7$ °C and $t_{AD}= 27.9$ °C temperatures and at atmospheric pressure $p_{atm}= 758.31$ mm/Hg atmospheric pressure.



Figure. 5. 4 Initial stage at the beginning of the experiment: a)-section of black steel sheet without corrosion; b)-top of the nozzle area, initially; c)-initial supply tank.

In Fig. 5.5 the state of the sheet metal surface exposed to the flow in the film is observed at 30 and 60 minutes respectively, with the presence of some altered areas on the sheet simultaneously with reaching the measured values. It is added that at the observed state the values from the meters corresponding to this operation time were $\sigma_{AD\ 0\ Gv\ I}=122.9\ \mu\text{S}/\text{cm}$, respectively $\sigma_{AD\ 0\ Gv\ I}=554\ \text{mV}$, at $t_{med\ atm}=26.9\ ^\circ\text{C}$ and $t_{AD}=27.1\ ^\circ\text{C}$ temperatures and at $p_{atm}=758.31\ \text{mm}/\text{Hg}$ atmospheric pressure.



Figure 5. 5 Experimental stage after 30-60 min: a) black steel sheet surface after 30 min; b) black steel sheet surface after 60 min; c) middle area after 60 min;

In the middle of the first experimental cycle, it is obvious the degree of advancement of the corrosion of the sheet metal section (Figure 5.7.), expressed simultaneously, quantitatively, by higher values of the conductivity, of $\sigma_{AD\ 46\ Gv\ I}=153\ \mu\text{S}/\text{cm}$ (respectively of the concentration of Fe total in the corrosion environment).

The end of the cycle is characterized by high values of conductivity, $\sigma_{AD\ 104\ Gv\ I}=170\ \mu\text{S}/\text{cm}$, $\sigma_{AD\ 104\ Gv\ I}=270\ \text{mV}$ respectively (Table 5.6.), a fact that clearly attests to the accumulation of Fe, hydroxyl, bicarbonate and carbonate ions in corrosion medium (water). Likewise, we present the values of the parameters recorded by the data logger (Figure 5.8), with $UR_{104\ Gv\ I}=56.4\%$ for relative humidity, $t_{S104}=25\ ^\circ\text{C}$, for system temperature, respectively $t_{PR104\ Gv\ I}=32.5\ ^\circ\text{C}$, for dew point temperature which overall characterizes the corrosion stage of the steel sheet surface (Figure 5.9), after exposure for a duration of 1440 min.



Figure 5. 7. Corrosion stage on black steel sheet surface on day III of the experimental study

Feeding flow $G_{VIAD} = 1.9 \text{ L/min}$										
Crt.no	Measurement range [min]	Sample collection interval [min]	Sample no.	Operating time	Pres. atm [mm/Hg]	Medium temp [C]	Water temp [C]	Elec. Cond. [$\mu\text{S/cm}$]	Ions content [mV]	
Ziua V										
88	0	n/a	n/a	n/a	n/a	744	25.5	25.9	175.1	250
89	15	1260	1	Top5 G v I	60	744.00	26.1	26.1	173.70	248.00
90	30					744.00	26.0	26.0	173.60	250.00
91	45					744.00	26.0	26.0	174.00	255.00
92	60					744.00	26.0	26.0	174.60	258.00
93	75	1320	2		12	744.00	25.9	25.8	174.90	258.00
94	90					744.00	25.9	26.0	175.50	260.00
95	105					744.00	26.0	25.8	175.80	265.00
96	120	1380	3		18	744.00	26.1	26.1	173.70	261.00
97	135					744.00	26.1	26.1	174.30	264.00
98	150					744.00	26.1	26.1	174.90	266.00
99	165			744.00		26.1	26.1	175.40	267.00	
100	180	1440	4	24	744.00	26.1	26.0	176.00	268.00	
101	195				744.00	26.1	25.9	176.20	269.00	
102	210				744.00	26.1	26.0	177.00	267.00	
103	225				744.00	26.1	26.0	177.40	267.00	
104	240					744.00	26.1	26.0	178.00	270.00



Figure 5.9 Corrosion stage on black steel sheet section on day V of the experimental study

At the end of subchapter 5.2, additional images from different experimental stages are presented.

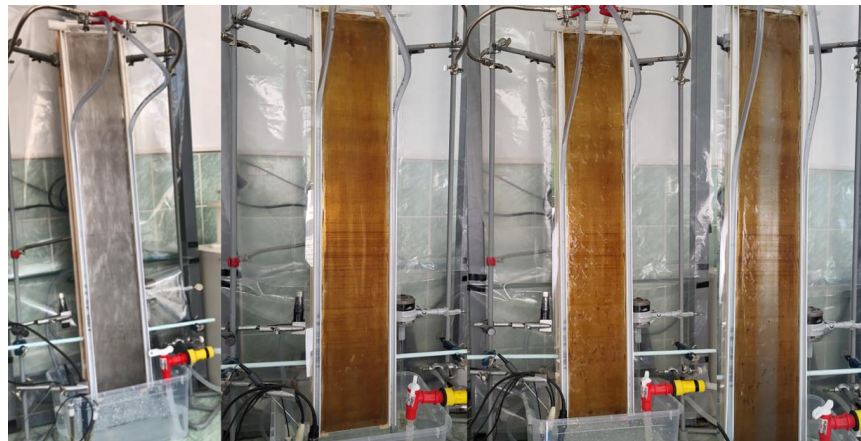


Figure 5.15 Corrosion stage in experimental research

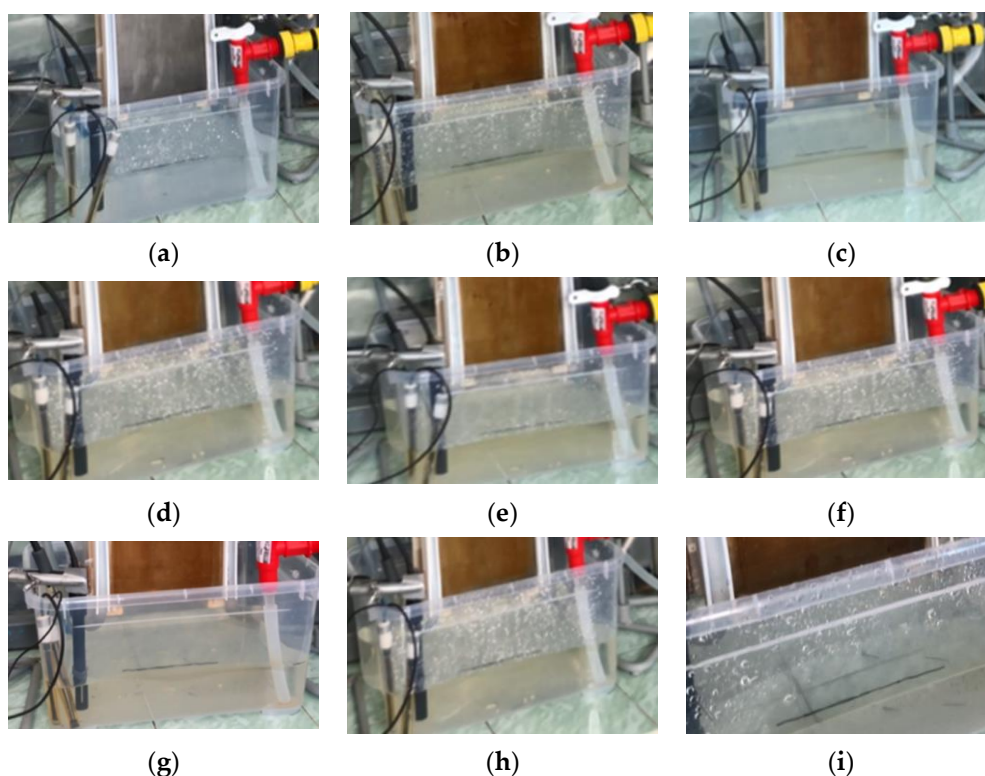


Figure 5.15 Stages of the corrosion environment in experimental corrosion research: a) initially; b) - i) with recirculated medium on the plate in corrosion stages

In subchapter 5.3, the experimental investigation and modeling of corrosion in film flow were presented, similar to how the results were published in *Metals* journal. In the *Abstract* it was shown that the experimental monitoring of corrosion dynamics in the film flow was carried out using a laboratory pilot model and that the mathematical model of the case takes into account the transfer of oxygen through the liquid film, which flows on the surface of the corroding plate, where they take place the characteristic surface chemical processes namely the dissolution of Fe , the oxidation of Fe^{2+} to Fe^{3+} and respectively the formation of surface deposits. Calculation of correlation coefficients for the apparent surface reaction rate constant and process factors showed that they correlate strongly and non-linearly with the *Reynolds* number (Re) for film flow, the cumulative flow duration, and the cumulative dwell time of the experiments. Using the dynamics of the resistance to oxygen transfer through the rust film and the dynamics of its thickness, resulting from the specific flux of rust deposition, the effective diffusion coefficient of oxygen through the rust film formed on the plate was expressed.

It is further specified how film corrosion occurs during rain, when a film of water is formed which flows on the surface of the metal in a downward flow. This film controls the transfer of oxygen from the air to the solid surface, where chemical (electrochemical) dissolution of the metal occurs. It is a complex process of diffusion, mass transfer and chemical reaction in which oxygen is the diffusible species, while the reactive species are, at the metal surface, water, oxygen and metal.

Figure 5.2 shows the importance of the research and presents (right side) at the same time some of the current procedures for surface protection against corrosion of any kind, not only that with the atmospheric environment as a source of reactive species on the surface.

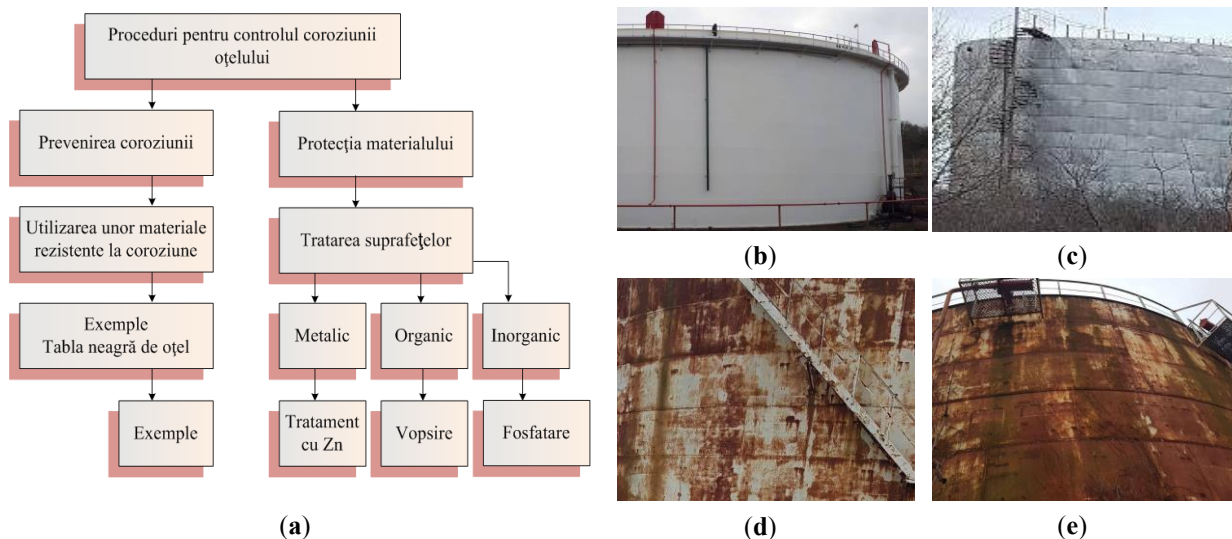


Figure 5. 2 Procedure for steel corrosion control and results of uncontrolled of film and drops corrosion of some tanks from an oil terminal: (a) stages of corrosion control; (b,c) tanks at the beginning of usage; (d,e) tanks after years of usage.

În Fig. 5.3, where the momentary elementary processes of corrosion by water droplets are presented, we observe:

1. An electrochemical process that identifies an anodic and a cathodic location, between which, the transfer of electrons takes place due to the corresponding cathodic and anodic reactions;

2. A mass transfer process through which oxygen reaches the liquid phase ($O_2(g) \rightarrow O_2$), to maintain the cathodic and anodic process;

3. A chemical reaction process, partly dependent on O_2 , which leads to the formation of rust on the steel surface ($Fe^{2+} + 2OH^- \rightarrow Fe(OH)_2$, $2Fe(OH)_2 + \frac{1}{2}O_2 + H_2O \rightarrow 2Fe(OH)_3$).

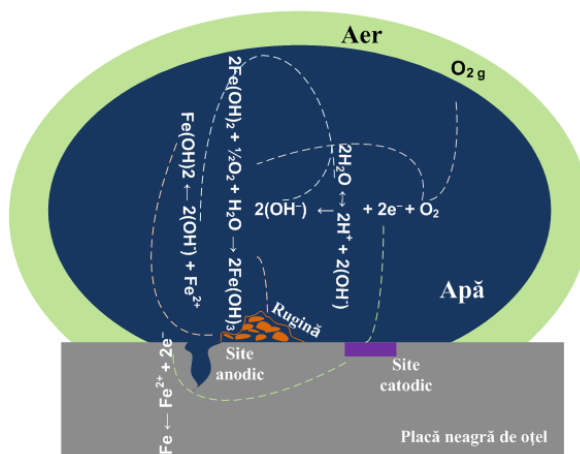
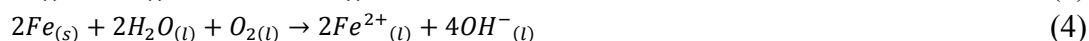


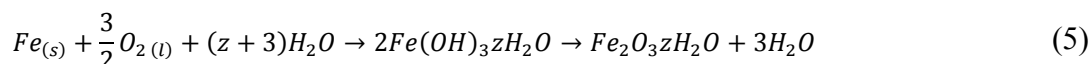
Figure 5. 3 Physical and chemical processes at atmospheric steel corrosion in a water drop.

If the ionization of water is expressed as a hydrogen (H⁺) ion generator as pointed out in Equation (1), it uses the anodic reaction (metal dissolution) in the form of Equation (2) and the cathodic reaction in the form of Equation (3); then, by summing them, Equation (4) is obtained.



From the point of view of chemical engineering, Equation (4) expresses a solid–liquid reaction, where it is obvious that the reaction itself (the sum of Equations (2) and (3)) takes place in active centers, as it does in heterogeneous catalysis. In this case, each reaction center consists of anodic and cathodic components. A consequence of this consideration is that this case can be treated kinetically with the methods specific to heterogeneous solid–liquid reactions.

In Equation (4), the kinetics of the process depends on the oxygen concentration in the liquid. This is strongly influenced by the transfer of oxygen from gas to liquid and from there to the cathodic side of the corrosion site. Now, it must be added that the mentioned heterogeneous process is, after oxygen, also under the influence of the local formation of rust points (centers). This could be associated with each corrosion center as shown by the heterogeneous reaction shown in Equation (5). It follows from Equation (4), to which the oxidation of Fe^{2+} to Fe^{3+} and the precipitation of the metal oxide are added, what are processes that occur outside or in the vicinity of the corrosion site.



In subchapter 5.3.2. the experimental installation and procedure are presented, and in Tab. 5.6 we find the composition of the steel sheet used in the experimental investigation of film corrosion (according to the manufacturer's data).

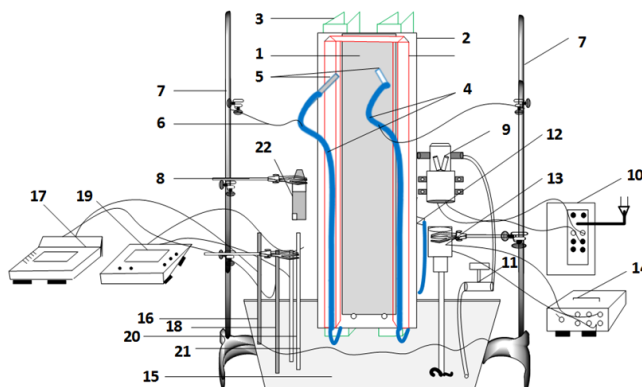


Figure 5. 4 Experimental laboratory setup for corrosion through a water flowing film: (1) surface of black steel sheet; (2) plastic plate support; (3) PVC strengthening supports; (4) water feed pipes; (5) water nozzles; (6) water pipe flexible supports; (7) laboratory stands; (8) clamps stands; (9) water pump; (10) current transformer for currents up to 12 V; (11) water flow rate control valve; (12) splitter for water pipes; (13) laboratory liquid mixer; (14) electric power supply for liquid mixer; (15) water tank; (16) MV ion selective electrode; (17) Fischer ion/pH selective device; (18) conductivity electrode; (19) conductivity meter; (20) temperature probe; (21) pH electrode; (22) air humidity data logger.

Tabelul 5. 1 Composition of black steel sheet used in film corrosion research (according to manufacturer).

Element	Composition (wt%)
Mangan (Mn)	0.166
Fosfor (P)	0.028
Sulf (S)	0.028
Carbon (C)	0.206
Crom (Cr)	0.078
Molibden (Mo)	0.114
Vanadiu (V)	0.003
Siliciu (Si)	0.004
Cupru (Cu)	0.082

Nichel (Ni)	0.088
Titan (Ti)	0.004
Fier (Fe)	0.199

It was further shown that the flux dynamics of surface-removed iron (N_{Fe}), for two consecutive measurements, can be calculated. Equation (6) was thus used, where c_{Ferzi} and $c_{Ferzi+1}$ are the iron concentrations of the corrosion medium at the corresponding times (τ_i and τ_{i+1}), and H and l are the height and width of the liquid film on the corrosion plate.

$$N_{Fe\ i} = \frac{V_l(c_{Ferzi+1} - c_{Ferzi})}{H l(\tau_{i+1} - \tau_i)} \quad (\text{Ec. 6})$$

Table 5. 2 Environmental conditions and data input for experimental investigation of steel corrosion in water falling film flow.

Exp. Nr.	$Re_b \delta, w_{max}, w, G_m$	pH	t_l °C	t_a °C	RH_a %	τ_d days	τ_e min	c_{elrx0} μS/cm	$c_{Fe\ rz0}$ mg/L
1	844.4	6.9	27.1	26.9	48.3	-	180	106	0
2	4.311×10^{-4} m	6.8	25.5	26.1	52.3	6	360	139	87
3	0.929 m/s	6.8	26.5	26.4	33.8	6	360	151	140
4	0.619 m/s	6.9	25.1	25.4	39.5	10	360	162	187
5	1.9 kg/min	6.7	22.9	23.6	58.4	8	240	175	242
6	400	6.7	23.7	23.9	43.7	25	170	97	0
7	3.361×10^{-4} m	6.9	22.5	23.1	41.5	15	300	103	6
8	0.567 m/s	6.9	21.3	21.7	53.2	9	360	120	38
9	0.368 m/s	7	21.5	22.1	42.7	11	200	160	72
10	0.9 kg/min	7.2	20.9	21.9	39.5	19	300	184	90
11	177.8	6.6	19.8	22.5	37.6	27	180	83	0
12	2.578×10^{-4} m	6.9	20.5	21.9	35.5	14	360	89	2.4
13	0.332 m/s	6.9	20.8	21.6	55.1	14	300	95	5
14	0.221 m/s	7.1	20.9	21.7	49.7	14	360	99	10
15	0.4 kg/min	7.1	21.2	22.3	47.9	7	260	104	15

(pH) corrosion water; (Gm) mass flow; (t_l) corrosion water temperature; (t_a) air environment temperature; (RH_a) relative air humidity; (τ_d) time from last experiment; (τ_e) time of active experiment; (c_{elrx0}) initial corrosion water electrical conductivity; ($c_{Fe\ rz0}$) initial iron content of corrosion water in device tank.

In subchapter 5.3.2.2. mathematical modeling was presented.

Regarding the processing of experimental measurements, the modeling problem consists in finding a coherent set of relations that express the dynamics of the concentration, $c_{Ferz(t)}$, and therefore implicitly the dynamics of the corrosion evolution on the plate, on which the film corrosion medium (N_{Fe}) flows in Eq. (6)). Figure 5.7 graphically introduces the description of the physical model that is considered here from the point of view of the transport, transfer and conservation of the oxygen species (O_2), without which the evolution of corrosion cannot take place. Figure 5.7 describes only part of the corrosion phenomenon on the corroded plate. Thus,

we see how the corrosion medium comes from the tank to the corrosion surface, with the oxygen concentration $c_{O_2rz(\tau)}$ and flows like a piston with speed w in a film of thickness δ . This fact corresponds to the situation where the flow on the flat plate is considered to be simplified, in that it is of piston type with the average velocity w , which in laminar flow is $2/3$ of the maximum surface velocity (w_{max}). Due to the evolution of corrosion, at the current position x along the corrosion surface the oxygen concentration decreases to the current mean value (c_{O_2}). For the control volume located between x and $x + dx$ there is oxygen supply with the N_{O_2} flow and oxygen consumption due to the surface reaction evolves with the specific surface velocity, V_{rsO_2} .

Here, oxygen consumption determines:

1. The removal of iron from the metal surface, as a result of the surface reaction;
2. The formation of $Fe_2O_3 \cdot H_2O$ horst;
3. The release of Fe ions into the corrosion medium.

Related to the control volume, the mentioned processes make the oxygen concentration at its exit $c_{O_2-dc_{O_2}}$. For the control volume, the oxygen balance for the unsteady state has the general form of Equation (7). This is transcribed into an analytical expression by Equation (8). Equation (9), which expresses the complete dynamics of the oxygen concentration near the surface subject to corrosion, results from dividing Equation (8) by the size of the control volume ($l \delta dx$).

$$\left(\begin{array}{c} \text{Debitul de oxigen} \\ \text{acumulat in v.c} \end{array} \right) = \left(\begin{array}{c} \text{Debitul de oxigen ce} \\ \text{iese din v.c} \end{array} \right) - \left(\begin{array}{c} \text{Debitul de oxigen ce vine} \\ \text{si respectiv pleaca din v.c} \end{array} \right) \quad (7)$$

$$l\delta dx \frac{\partial c_{O_2}}{\partial \tau} = wl\delta(c_{O_2} - dc_{O_2}) - V_{rsO_2}l\delta x - wl\delta dc_{O_2} + N_{O_2}l\delta x \quad (8)$$

$$\frac{\partial c_{O_2}}{\partial \tau} + w \frac{\partial c_{O_2}}{\partial x} = \frac{1}{\delta}(N_{O_2} - V_{rsO_2}) \quad (9)$$

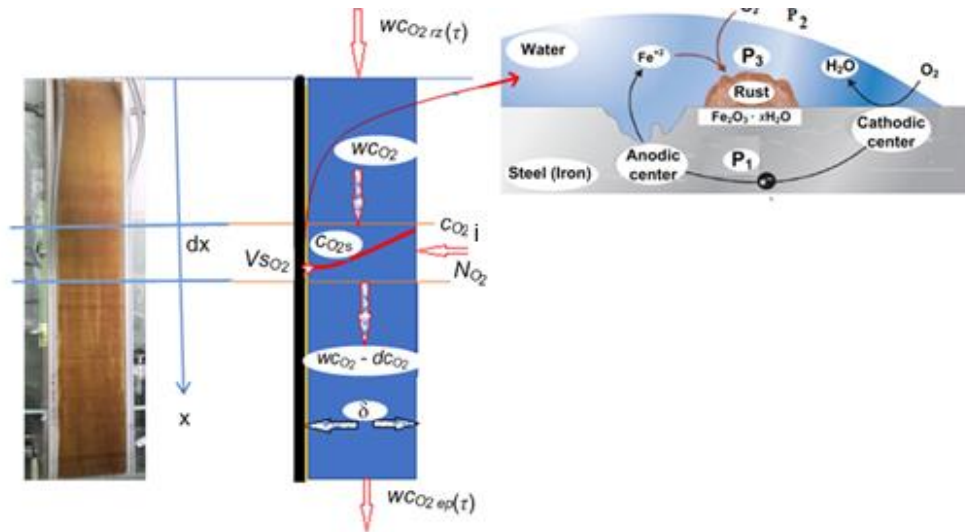


Figure 5.5 Vertical film flow corrosion model for black steel plate (O₂ balance, at the beginning of corrosion; P₁—electrons transfer between anodic and cathodic points, P₂—oxygen absorption, P₃—rust production).

An addition to Equation (8) takes into account reverse flow, which occurs due to surface roughness or the formation of flow microwaves. It is phenomenologically characterized by the meaning of the axial mixing coefficient D_L . Completion of Equation (9) forms Equation (10). This form still needs to be completed, as shown below, by taking into account the consumption of oxygen by the oxidation of Fe^{2+} ions.

$$\frac{\partial c_{O_2}}{\partial \tau} + w \frac{\partial c_{O_2}}{\partial x} = D_L \frac{\partial^2 c_{O_2}}{\partial x^2} + \frac{1}{\delta}(N_{O_2} - V_{rsO_2}) \quad (10)$$

Equation (10) requires computational models or expressions for δ , w_{max} , w , D_L , N_{O_2} and V_{rsO_2} .

When the mass flow rate is imposed by the film thickness (Equation (11)), the maximum superficial velocity (Equation (12)) and the mean velocity in the film (Equation (13)) are

expressed by analogy with a laminar flow on a vertical plate [20, 21] (where η is the corrosion water viscosity; g is the gravitational acceleration; and ρ is the corrosion water density).

$$\delta = \sqrt[3]{\frac{3\eta G_m}{\rho^2 g l}} \quad (11)$$

$$w_{max} = \frac{\delta^2 g \rho}{2\eta} \quad (12)$$

$$w = \frac{2}{3} w_{max} = \frac{\delta^2 g \rho}{3\eta} \quad (13)$$

The oxygen flux passing through the film towards the corroded surface is given by Equation (14), with the mass transfer coefficient expressed in Equations (15) and (16), as an average value, according to the penetration theory [22] or according to the Johnstone model and Pigford [23]

$$N_{O_2} = k_l (c_{O_2i} - c_{O_2s}) \quad (14)$$

$$k_l = 2 \sqrt{\frac{D_{O_2} w_{max}}{\pi H}} \quad (15)$$

$$k_l = 3.41 \frac{D_{O_2}}{\delta} \quad (16)$$

Experimental observations led to the conclusion that the appearance and development of corrosion centers follow an evolution both in time and in the x -axis direction. In fact, the maximum fraction of surface area occupied by the crust (ϵ_{max}) is obtained after a sufficient time from the start of corrosion in the film. Thus, the surface reaction rate, $\text{kg}_{O_2}/(\text{m}^2 \cdot \text{s})$, is expressed by Equation (17), where α is a dimensional constant T^{-1} , and the function $f(x, \tau)$ in Equation (18) tries to describe coverage of corrosion centers along the x -axis. It should also be noted that in the kinetic expression, the surface reaction rate constant (k) has the dimension LT^{-1} , that is, the dimension of a mass transfer coefficient.

$$V_{SO_2}(x, \tau) = (1 - e^{-\alpha\tau}) f(x) \epsilon_{max} k_{rs} c_{O_2s} \quad (17)$$

$$f(x) = \begin{cases} 1 + \frac{x}{L} - \left(\frac{x}{L}\right)^2, & 1 - e^{-\alpha\tau} < 0.98 \\ 1, & 1 - e^{-\alpha\tau} \geq 0.98 \end{cases} \quad (18)$$

The flux of dissolved iron, in position x and time τ , becomes based on the stoichiometry of Equation (4). It is given by Equation (19). The stoichiometry in Equation (5) shows how we can establish the deposition flux of ferric hydroxide hydrate from Equation (20), which is actually the flux showing rust development ($Fe_2O_3 \cdot zH_2O$). In Equation (20), the degree of Fe^{2+} oxidation (η_{rox}) is a process parameter.

$$N_{Fe}(x, \tau) = \frac{4}{3} \frac{V_{SO_2}(x, \tau)}{M_{O_2}} M_{Fe} \quad (19)$$

$$N_{Fe(OH)_3}(x, \tau) = \eta_{rox} N_{Fe}(x, \tau) \frac{M_{Fe(OH)_3 \cdot 3H_2O}}{M_{Fe}} \quad (20)$$

To determine how the iron ions reach the corrosion water (environment), it must be checked whether they ($pH = 6.9-7.2$, $t = 25^\circ\text{C}$) can react with the Fe^{2+} ions as Fe^{3+} ions. We thus start from the fact that $Fe(OH)_3$ has, at 291 K, a value of the solubility product $P_s = 1.1 \times 10^{-36}$. According to this P_s value, it follows that from any location on the corrosion surface, where it is $Fe(OH)_3 \cdot zH_2O$ (actually $Fe_2O_3 \cdot zH_2O$), the concentration of trivalent iron ions on the corrosion surface is calculated according to the established Equations (21)–(24).



$$c_{OH} = 3c_{Fe3} \quad (22)$$

$$P_s = (c_{Fe3})(c_{OH})^3 = 27(c_{Fe3})^4 \quad (23)$$

$$c_{Fe3} = \left(\frac{P_s}{27}\right)^{0.25} = \left(\frac{1.1 \times 10^{-36}}{27}\right)^{0.25} = 4.5 \times 10^{-10} \frac{moli}{L} = 2.62 \times 10^{-8} g/L \quad (24)$$

This value of c_{Fe3} , namely 2.62×10^{-8} g/L, makes the specific transfer flow to the corrosion medium around 2.62×10^{-13} kg $_{Fe3}$ /(m²s). This low concentration of Fe^{3+} in the corrosion medium cannot support the strong increase in its electrical conductivity. For a corrosion surface of 0.15 m² and 5 L of recirculated water, the flow rate of Fe^{3+} ions coming out of the plate reaches 3.93×10^{-14} kg $_{Fe3}$ /s and the duration to obtain the Fe^{3+} precipitation concentration in the corrosion medium is $\tau_p = (Vc_{Fe3})/(3.93 \times 10^{-14}) = 3.325 \times 10^3$ s. Our observations showed that this time of appearance of $Fe(OH)_3$ in the recirculated medium is shorter, not exceeding 2000 s. The explanation lies in the oxidation of Fe^{2+} ions, released by corrosion, which reach this medium. According to Equation (20), we can write that the specific Fe^{2+} flow coming into the corrosion medium can be expressed as Equation (25). Inside the corrosion environment, where oxygen exists, Fe^{2+} is oxidized, as shown in Equation (26), to Fe^{3+} , which then precipitates as $Fe(OH)_3$.

$$N_{Fe2}(x, \tau) = (1 - \eta_{rox})N_{Fe}(x, \tau) \quad (25)$$



The kinetics of the homogeneous oxidation in water of Fe^{2+} to Fe^{3+} is expressed [24-26] in the form of Equation (27). Here, PO_2 is the partial pressure of oxygen in the air at the air/water interface and c_{OH^-} and c_{Fe2+} are the corresponding ion concentrations in the water. If we consider the partial pressure of O_2 air in the atmosphere, a temperature of 25 °C, a pH interval of 6.5–7.5, and the ion concentrations expressed in mol/L, then the kinetic constant k_{ox} has the value 3.33×10^{11} L/(atm·mol·s).

$$-\frac{dc_{Fe2+}}{d\tau} = k_{ox}c_{Fe2+}(c_{OH^-})^2P_{O_2} \quad (27)$$

If the corrosion medium also contains other important ions, such as Na^+ and Cl^- (cases of corrosion in slightly saline water), or even different ones, then the elementary processes that accelerate corrosion must also be identified and, taking this into account, additions to Equations (19) and (28) must then be made accordingly. However, this is not the case in the current investigation. In our case, expressing c_{OH^-} from the ionic product of water (Equation (22)), we will have, at 25 °C, atmospheric pressure, and $pH = 7$, a value for c_{OH^-} of 10^{-7} mol/L. Now, taking $PO_2 = 0.21$ atmospheres, Equation (27) becomes Equation (28), a first-order kinetic relationship with respect to c_{Fe2+} , where the value 15.76×10^{-3} s⁻¹ is for the reaction constant k_{oxr} . To express c_{Fe2+} in kg $_{Fe2+}$ /m³, the right side of the expression is multiplied by the Fe molecular mass.

$$-\frac{dc_{Fe2+}}{d\tau} = v_{rFe2+} = k_{oxr}c_{Fe2+} M_{Fe} \quad (28)$$

The above data show that the O_2 balance must be completed, in relation to the control volume considered in Figure 5.7, with O_2 consumption for Fe^{2+} oxidation. According to the stoichiometry of the reaction from Equation (26) and according to the Fe^{2+} oxidation kinetics, the evolution of oxygen consumption in the corrosion medium has the expression from Equation (29). Figure 5.8 shows the mentioned completion and Equation (30) expresses the dynamics of the mean oxygen concentration in the film at position x and time τ . If it is admitted that the precipitation of $Fe(OH)_3$ is fast, then we will not have Fe^{3+} in solution above 2.68×10^{-8} g/L (see above). So, in the liquid phase, we have both Fe^{2+} ions and $Fe(OH)_3$ micro particles resulting

from Fe^{2+} oxidation. Consequently, for the considered control volume, their balance must be added. Figure 5.9 shows the description of the Fe^{2+} and $Fe(OH)_3$ balances.

$$v_{rO_2} = \frac{1}{4} v_{rFe^{2+}} \frac{M_{O_2}}{M_{Fe}} \quad (29)$$

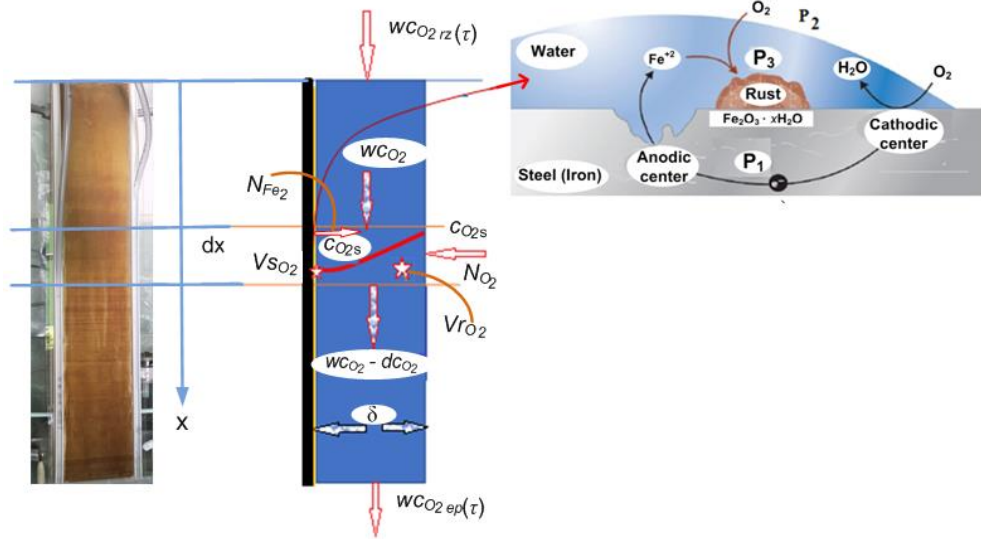


Figure 5. 6 Vertical film flow corrosion model for steel plates (complete O₂ balance; P1—electrons transfer between anodic and cathodic points, P2—oxygen absorption, P3—rust production).

$$\frac{\partial c_{O_2}}{\partial \tau} + w \frac{\partial c_{O_2}}{\partial x} = D_L \frac{\partial^2 c_{O_2}}{\partial x^2} + \frac{1}{\delta} \left(N_{O_2} - V_{SO_2} - N_{Fe(OH)_3} \frac{M_{O_2}}{4M_{Fe(OH)_3 \cdot 3H_2O}} \right) - v_{rO_2} \quad (30)$$

The particularization of Equation (7) for Fe^{2+} for the $Fe(OH)_3$ balance leads to the partial differential equations (Equation (31) and (32)), which express the dynamics of the concentration of these species on the corroding plate. Here, we maintain the plug flow through axial mixing for the flowing liquid.

$$\frac{\partial c_{Fe^{2+}}}{\partial \tau} + w \frac{\partial c_{Fe^{2+}}}{\partial x} = D_L \frac{\partial^2 c_{Fe^{2+}}}{\partial x^2} + \frac{1}{\delta} N_{Fe_2} - v_{rFe^{2+}} \quad (31)$$

$$-\frac{\partial c_{Fe(OH)_3}}{\partial \tau} + w \frac{\partial c_{Fe(OH)_3}}{\partial x} = D_L \frac{\partial^2 c_{Fe(OH)_3}}{\partial x^2} + \frac{M_{Fe(OH)_3}}{M_{Fe}} v_{rFe^{2+}} \quad (32)$$

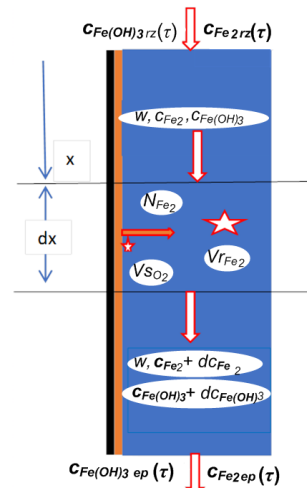


Figure 5. 7 Vertical film flow corrosion model for steel plates (Fe^{2+} and $Fe(OH)_3$ balance).

The general mathematical model of the process taking place on the plate contains the partial derivative equations (Equations (30)–(32)) with explanatory relationships for the reaction rate of oxygen consumption at the corrosion surface (V_{sO_2}), for the specific oxygen flow rate to the corrosion surface (N_{O_2}), for the reaction rate of oxygen consumption in the oxidation of Fe^{2+} (v_{rO_2}), for the specific flow rate of Fe^{2+} coming into the liquid ($N_{Fe^{2+}}$), and for the oxidation rate of Fe^{2+} in liquid ($v_{rFe^{2+}}$).

The model can be customized by attaching to it the univocity conditions expressed in Equations (33)–(35).

$$\tau = 0, x \geq 0, c_{O_2} = c_{O_2i}, c_{Fe^{2+}} = 0, c_{Fe(OH)_3} = 0 \quad (33)$$

$$\begin{aligned} \tau > 0, \quad x = 0, \quad D_L \frac{dc_{O_2}}{dx} &= w(c_{O_2 r_z}(\tau) - c_{O_2 r_z \tau}), D_L \frac{dc_{Fe^{2+}}}{dx} \\ &= w(c_{Fe^{2+}}(\tau) - c_{Fe^{2+} r_z \tau}), D_L \frac{dc_{Fe(OH)_3}}{dx} \\ &= w(c_{Fe(OH)_3}(\tau) - c_{Fe(OH)_3 r_z \tau}) \end{aligned} \quad (34)$$

$$\tau > 0, \quad x = H, \quad \frac{dc_{O_2}}{dx} = 0, \frac{dc_{Fe^{2+}}}{dx} = 0, \frac{dc_{Fe(OH)_3}}{dx} = 0 \quad (35)$$

It should be specified that Equation (34) is a univocity condition of the specified three-concentration field Equations (30)–(32) and a link relationship [24] between the corrosion model on the plane plate and the unsteady-state operation model of chemical processes in the corrosion medium tank. Regarding the processes that take place in the corrosion medium in the recirculation tank, Figure 5.8 tries to show their phenomenology. Here, we note that the perfect mixing flow model is accepted and that oxygenation of the corrosion medium occurs through the free surface. Also, the oxidation of Fe^{2+} continues and due to this oxidation, the generation of ferric hydroxide increases in intensity.

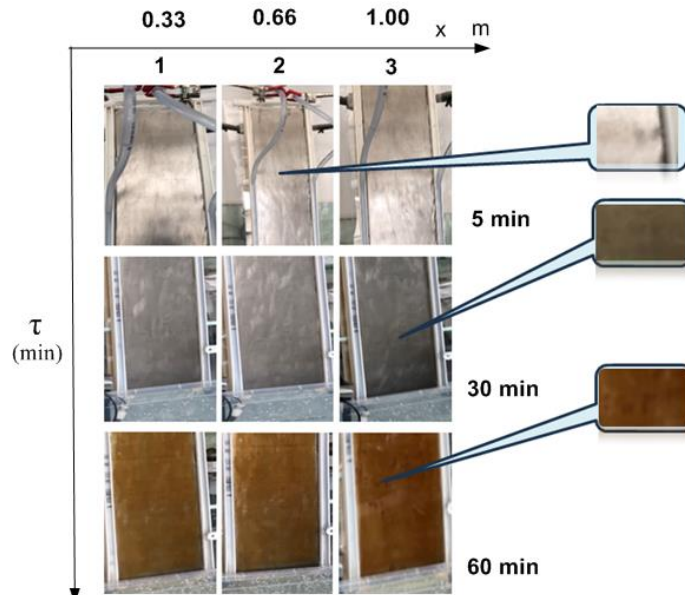


Figure 5. 8 Corrosion evolution in time and space at the beginning of the process ($1 - x = (0 - 0.33 \text{ m})$, $2 - x = (0.33 - 0.66 \text{ m})$, $3 - x = (0.66 - 1 \text{ m})$).

The characteristic equations of the processes in the recirculation tank of the corrosion medium are the three unsteady-state balance equations for oxygen (Equation (36)), Fe^{2+} ions (Equation (37)) and $Fe(OH)_3$ micro precipitate (Equation (38)). For these ordinary differential equations, the initial conditions in Equation (39) are used.

$$\frac{dc_{O_2\ rz}}{d\tau} = \frac{G_{vl}}{V_{rz}}(c_{O_2\ ep} - c_{O_2\ rz}) + \frac{S_{lb}}{V_{rz}}N_{O_2\ rz} - \frac{1}{4}v_{rFe2rz}\frac{M_{O_2}}{M_{Fe}} \quad (36)$$

$$\frac{dc_{Fe^{2+}\ rz}}{d\tau} = \frac{G_{vl}}{V_{rz}}(c_{Fe\ ep^{2+}} - c_{Fe\ rz^{2+}}) + v_{rFe2rz} \quad (37)$$

$$\frac{dc_{Fe(OH)_3\ rz}}{d\tau} = \frac{G_{vl}}{V_{rz}}(c_{Fe(OH)_3\ ep} - c_{Fe(OH)_3\ rz}) + v_{rFe2rz}\frac{M_{Fe(OH)_3}}{M_{Fe}} \quad (38)$$

$$\tau = 0, \quad c_{O_2\ rz} = c_{O_2\ i} = 8\frac{mg}{L}, \quad c_{Fe^{2+}} = 0, \quad c_{Fe(OH)_3} = 0 \quad (39)$$

Therefore, the mathematical model of corrosion in film flow, coupled to the working mode of the experimental laboratory installation described above, contains the set of partial and ordinary derivative equations (Equations (30)–(39)). Added to this are the relationship expressions for V_{sO_2} , N_{O_2} , v_{rO_2} , and $v_{rFe^{2+}}$. The dynamics of the specific flow rate of dissolved iron (N_{Fe}), the dynamics of the specific flow rate of ferric hydroxide ($N_{Fe(OH)_3}$), which is deposited as rust, and the dynamics of the specific flow rate of Fe^{2+} ions ($N_{Fe^{2+}}$) are also of interest. They are related to each other and depend on the rate of the surface reaction (V_{sO_2}).

There are 4 parameters in the model that require identification, namely α , k_{rs} , and ε_{max} in the V_{sO_2} expression (Equation (17)), and the Fe^{2+} oxidation yield (η_{ox}) in the $N_{Fe(OH)_3}$ expression (Equation (20)).

Subchapter 5.3.2.3 presented the results of the experimental study. We found that for $\tau = 1$ h, the surface of the iron plate was completely covered with active centers (Figure 5.10). Thus from relation (17) $(1 - e^{-\alpha\tau})f(x)$ goes to 1 around one hour, which requires $\alpha = 3.91\text{ h}^{-1}$. This observation also complements and clarifies the initial and uniqueness conditions of the entire corrosion model.

Following the coverage of the surface with active corrosion centers, the relation for $V_{sO_2}(x, \tau)$ becomes as in Equation (40). Here the apparent surface reaction constant k'_{rse} takes into it the fraction of surface occupied by horsts (ε_{max}) and the effect of blocking corrosion by increasing the thickness of the horst film surface.

$$V_{sO_2}(x, \tau) = k'_{rse}c_{O_2s}(x, \tau) \quad (40)$$

Table 5.2 summarizes the concrete conditions of each experiment at the beginning and during its evolutions.

For each experiment, the dynamics of the electrical conductivity of the corrosion medium and the dynamics of its total Fe content are shown in Figures 5.13–5.18. First of all, for the purposes of this paper, we showed that each pair $(c_{el\ rz}, c_{Fe\ rz})$ of the 15 pairs of corrosion dynamics curves can be interpreted by the presented model, so that k'_{rse} and η_{rox} can be determined for each specific case. To justify the previous statement, we state that we have shown that the steel film corrosion model has four parameters, and we have shown that α has been identified and ε_{max} has been merged into the surface reaction rate constant.

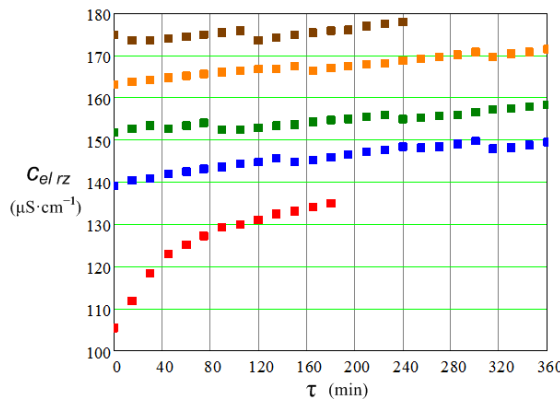


Figure 5.13 Dynamics of electrical conductivity of corrosion water from the 5 experiments with a liquid flow rate of 1.9 L/min ($Re_l = 844.4$).

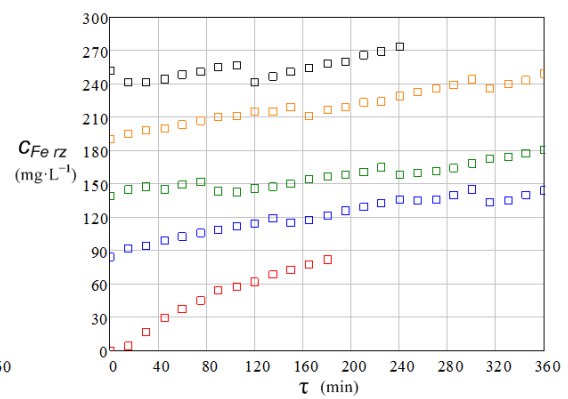


Figure 5.14 Dynamics of the total iron content of the corrosion water from the 5 experiments with a liquid flow rate of 1.9 L/min ($Re_l = 844.4$).

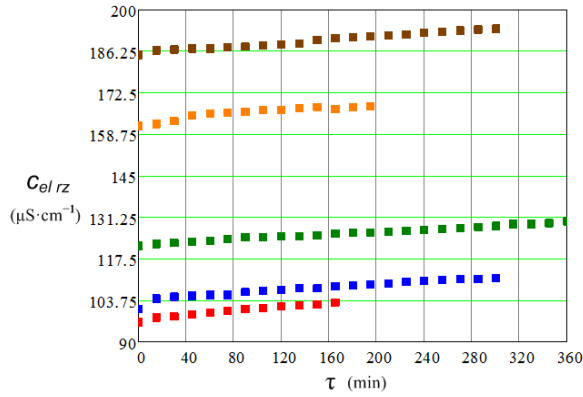


Figure 5.15 Dynamics of electrical conductivity of corrosion water from the 5 experiments with a liquid flow rate of 0.9 L/min ($Re_l = 400$).

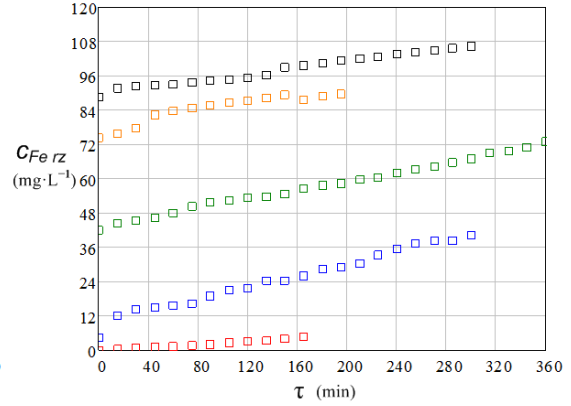


Figure 5.16 Dynamics of the total iron content of the corrosion water from the 5 experiments with a liquid flow rate of 0.9 L/min ($Re_l = 400$).

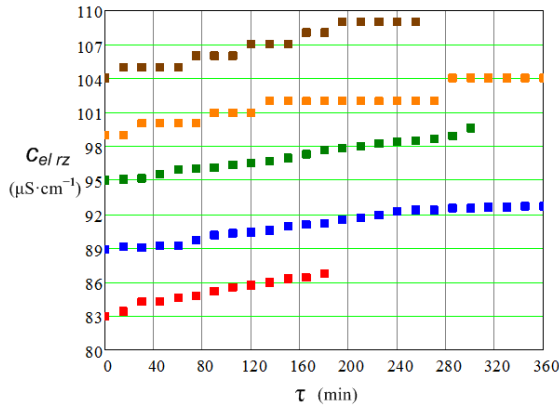


Figure 5.17 Dynamics of electrical conductivity of corrosion water from the 5 experiments with a liquid flow rate of 0.4 L/min ($Re_l = 177.8$).

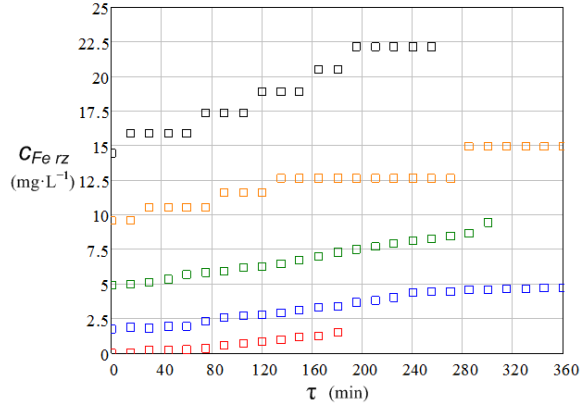


Figure 5.18 Dynamics of the total iron content of the corrosion water from the 5 experiments with a liquid flow rate of 0.4 L/min ($Re_l = 177.8$).

A quick look at the $c_{el\ r_z}$ vs. τ and $c_{Fe\ r_z}$ vs. τ curves can clearly distinguish that the first experiment that started with the virgin steel plate is characterized by the strongest dynamics (e.g., the $c_{el\ r_z}$ increased by 45 $\mu\text{S}/\text{cm}$ in 180 min and the $c_{Fe\ r_z}$ has an increase of 82 mg/L in 180 min (red curve in Figures 10 and 11) versus an increase in $c_{el\ r_z}$ of 11 $\mu\text{S}/\text{cm}$ in 360 min and an increase in $c_{Fe\ r_z}$ of 33 mg/L in 360 min (green curve in Figures 5.15 and 5.16)).

A comparison of the 15 experiments of active corrosion in the flowing film can be made by analyzing the dynamics of the flow of steel away from the plate, as well as its average maximum and minimum values. Thus, the data sets $c_{Fe\ r_z}$ vs. τ were analytically transformed by a polynomial dependence of the 3rd degree and the specific corrosion flow rate, given by Equation (6), was expressed accordingly. Figure 5.19 and Table 5.3 show the result of this data processing. Table 3 also contains the data for the mean specific steel flow rate obtained with a linear relationship $c_{Fe\ r_z}$ vs. τ , which is supported by the shape of the curves shown in Figures 5.13 - 5.18.

Figure 5.19 și Table 5.3 show that:

1. The specific corrosion flow rate vs. the time dependences in 5.19 decreased linearly and increased nonlinearly, with a maximum or a minimum due to the relationship of $c_{Fe\ r_z}$ vs. τ by a polynomial with a 3rd degree of dependence;
2. It is interesting to note that the integral average values of the specific corrosion flow rate were very close to those where the dependence of $c_{Fe\ r_z}$ vs. τ was linear (columns 5 and 6 of Table 5.3);
3. The first experiment is distinguished, compared to all the others, by the dynamics of $c_{Fe\ r_z}$ vs. τ and by the very high values of the specific flow; here, at $Re_l = 844.7$ in 180 min, a $c_{Fe\ r_z}$ of 80 mg/L was reached and the mean specific steel corrosion rate was 15.61 $\text{mg}/(\text{m}^2 \cdot \text{min})$, compared to experiment 5 where $c_{Fe\ r_z}$ increased in 240 min, with a $c_{Fe\ r_z}$ of 30 mg/L with a mean flow rate specific to iron corrosion of 3.532 $\text{mg}/(\text{m}^2 \cdot \text{min})$;

4. These results support the previous observation which showed that the reduction of the specific flow of iron away from the plate is the consequence of the thickening of the rust layer on its surface.

Table 5. 3 Values for specific flow rate of iron for all active experiments.

Exp. Nr.	Liquid flow	$N_{Fe \text{ min}}$	$N_{Fe \text{ max}}$	$N_{Fe \text{ mediu}}^1$	$N_{Fe \text{ mediu}}^2$
		$\frac{\text{mg}}{\text{m}^2 \cdot \text{min}}$	$\frac{\text{mg}}{\text{m}^2 \cdot \text{min}}$	$\frac{\text{mg}}{\text{m}^2 \cdot \text{min}}$	$\frac{\text{mg}}{\text{m}^2 \cdot \text{min}}$
1	$G_{vl} = 1.9$ L/min	8.62	25.7	15.61	15.386
2	$Re_l = 844.4$	0.55	8.97	5.06	5.115
3		1.9	7.22	3.47	3.325
4		5.02	7.32	5.25	4.961
5		0.55	14.25	3.88	3.353
6		$G_{vl} = 0.9$ L/min	0.53	1.11	0.928
7	$Re_l = 400.0$	3.15	5.15	3.728	3.567
8		2.39	3.89	2.849	2.676
9		0.52	5.15	1.822	2.525
10		1.37	2.15	1.822	1.918
11		$G_{vl} = 0.4$ L/min	0.05	0.31	0.276
12	$Re_l = 177.8$	0.11	0.38	0.323	0.323
13		0.38	0.55	0.478	0.475
14		0.32	0.94	0.561	0.495
15		0.17	1.36	0.996	1.091

¹ Integral mean value with 3rd degree polynomial dependence $c_{Fe \text{ rz}}$ vs. τ ; ² integral mean values with linear dependence $c_{Fe \text{ rz}}$ vs. τ .

None of the 15 reported experiments showed a sudden increase in the iron content in the corrosion medium, a fact that would show an important degradation of the rust film formed on the surface. Given the random distribution of time duration between experiments, this observation may be a sign that between two rainfall events, the rust layer on an attacked surface does not change its state or even its structure.

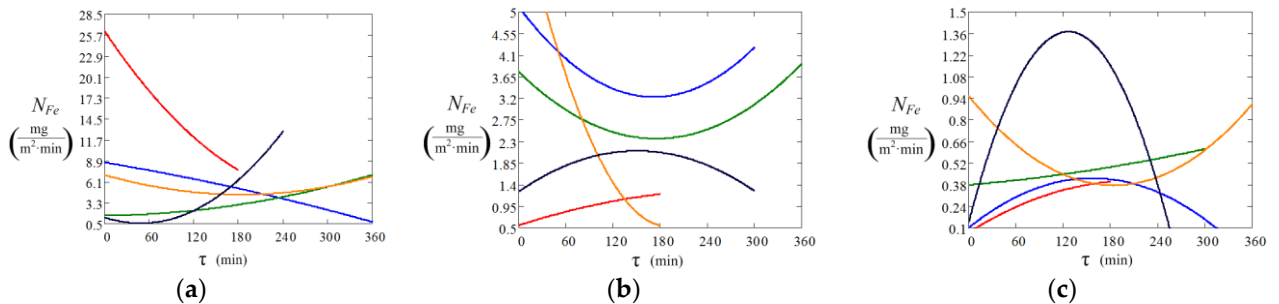


Figure 5. 9 Dynamics of corrosion specific flow rate for experiments with (a) liquid flow rate of 1.9 L/min, (b) liquid flow rate of 0.9 L/min; (c) liquid flow rate of 0.4 L/min (colors correspond to those in Figures 5.13–5.18).

In subchapter 5.3.2.4. the validation of the mathematical model was discussed based on the experimental measurements presented above, for which the following procedure was used to determine the two parameters of the model:

- The mathematical model was transposed into a numerical form as a function dependent on the parameters to be identified, namely k'_{rse} and η_{rox} ;
- The mentioned parameters were identified for all experiments using the minimization of the root mean square deviation (Equation (41)) between the values regarding the dynamics of the

corrosion steel content in the medium that were calculated by the model and those measured experimentally [29, 30]

• From the identified values of the apparent surface reaction rate constant, the increase in oxygen mass transfer resistance due to the rust layer was determined by Equation (42), where R_{sfr} is the surface reaction resistance and R_{rul} is the mass transfer resistance of the rust layer.

$$F(k'_{rse}, \eta_{ox}) = \sum_{i=1}^N (c_{Fe\ r_z}(k'_{rse}, \eta_{ox}, \tau_i) - c_{Fe\ r_z\ ex}(\tau_i))^2 \quad (41)$$

$$R_T = R_{sfr} + R_{rul} \quad (42)$$

Table 5.4 contains the values of the identified values for k'_{rse} and η_{ox} for all the developed experiments. In the numerical expression of $c_{Fe\ r_z}(k'_{rse}, \eta_{ox}, \tau_i)$, the axial dispersion coefficient was estimated to be 1.7×10^{-6} m²/s for $Re_l = 844.4$, with a linear decrease for the other Re_l values. It should also be noted that testing the sensitivity of the numerical model for the range $D_L 10^{-5}$ – 10^{-7} m²/s showed an extremely small influence of this parameter on the dynamics of the investigated process. The k'_{rse} and η_{ox} values, derived from the minimization of the mean squared deviation, have the quality of being maximum confidence values [30, 31]

In Table 5.4, among the factors influencing the two parameters, the liquid flow rate, the cumulative duration of the film flow on the sample surface (τ_f), as well as the resting time (τ_d) were considered.

Table 5. 4 The identified values of k'_{rse} , η_{ox} , and their external factors (t_a and t_l : 21–27 °C, RHa : 35–55%)

Exp. Nr.	Liquid flow	Film flow time τ_f (h)	τ_d (days)	$k'_{rse} 10^{-5}$ m/s	η_{ox} -	$R_T 10^{-5}$ s/m	$R_{rul} 10^{-5}$ s/m	Fig. 5.19 *
1		3	-	2.296	0.19	0.455	0	(a) E1
2	$G_{vl} = 1.9$	9	6 (6)	0.716	0.18	1.397	0.941	(a) E2
3	L/min	15	6 (12)	0.506	0.16	1.976	1.521	(a) E3
4	$Re_l = 844.4$	21	10 (22)	0.496	0.16	2.004	1.548	(a) E4
5		25	8 (30)	0.358	0.16	2.793	2.338	(a) E5
6		28	25 (55)	0.155	0.18	6.061	5.605	(b) E1
7	$G_{vl} = 0.9$	33	15 (70)	0.425	0.18	2.353	1.897	(b) E2
8	L/min	41	9 (79)	0.336	0.17	2.976	2.521	(b) E3
9	$Re_l = 400.0$	44	11 (90)	0.315	0.15	3.175	2.719	(b) E4
10		49	19 (109)	0.298	0.17	3.356	2.899	(b) E5
11		52	27 (135)	0.051	0.17	18.179	17.132	(c) E1
12	$G_{vl} = 0.4$	58	14 (149)	0.032	0.14	29.411	28.861	(c) E2
13	L/min	63	14 (163)	0.043	0.16	23.258	22.796	(c) E3
14	$Re_l = 177.8$	69	14 (177)	0.057	0.17	17.54	17.089	(c) E4
15		74	7 (184)	0.106	0.16	9.434	8.978	(c) E5

* From Figure 17: (a) E1–E5 experiments; (b) E1–E5 experiments; (c) E1–E5 experiments.

The consideration of the flow rate of the liquid, by itself or the Re_L number, as an influencing factor on k'_{rse} and η_{rox} comes from the fact that it influences the diffusion of oxygen through the liquid film and through the surface of the rust crust at the corrosion centers.

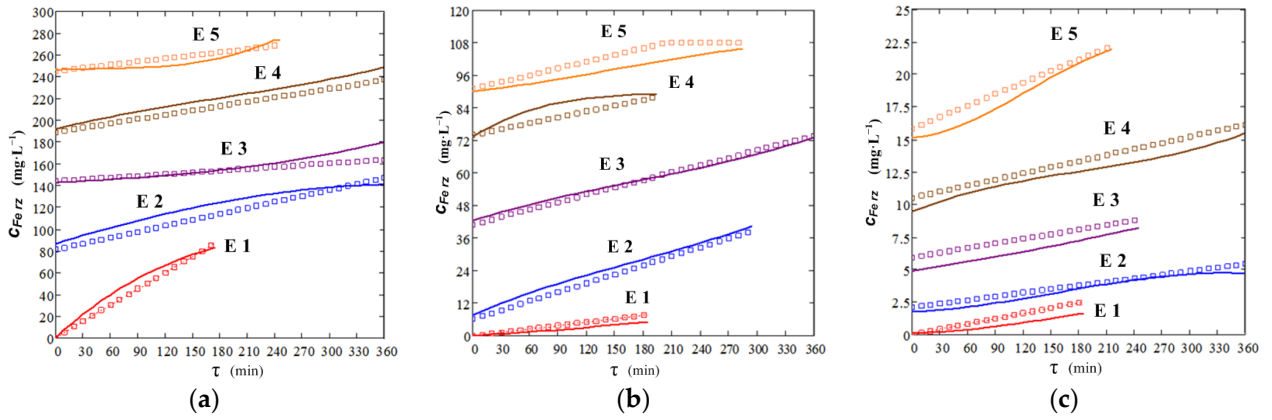


Figure 5.10 Dynamics of total iron content in corrosion water from experiments and according to the model, with parameters from Table 5.4 (*line*—experimental data, *points*—model computed data): (a) $Re_l = 844.4$, (b) $Re_l = 400$, (c) $Re_l = 177.8$, t_a and t_f : 21–27 °C, RH_a : 35–55%.

As expected, the apparent surface reaction constant showed high values when the rust film did not actually exist on the surface (2.129×10^{-5} m/s in experiment number 1). These values decreased close to 70 times when the rust film and its age were large (0.032×10^{-5} m/s in experiment number 12). The apparent constant for surface reaction correlates well (Table 5.5) with the influencing factors in Table 5.4. This fact quantitatively confirms that the process of surface film flow corrosion has a surface kinetic component, via the diffusion of oxygen through the rust film in the active process and the densification of the rust film (increasing the resistance of the structure to oxygen or to the diffusion of iron ions in the wet film) during the waiting period. Figure 5.20 shows the excellent coverage of the film corrosion dynamics measurements by the model using the parameter values in Table 5.4. Through these correlations, we have shown how the three factors influence the surface reaction rate constant and hence, the momentary corrosion speed. Many works have shown the influence of superficial flow [32, 33] on the corrosion of steel or alloys. Similarly, in atmospheric corrosion, the rust layer formation on the corrosion surface reduces the corrosion speed ($v_c = kt^n$ with n subunit [34])

Table 5.5 Correlation coefficients for k'_{rse} and $\ln(k'_{rse})$ and process factor from Table 5.4.

Correlation Coefficient	Reynolds Number Re_l	Film Flow Time τ_f (h)	Standby Time τ_d (days)
k'_{rse}	0.649	-0.712	-0.649
$\ln k'_{rse}$	0.848	-0.872	-0.873

The different behaviors of the rust film in the diffusion of oxygen to the surface reaction are highlighted by the graphical representation shown in Figure 5.21. Here, the mean thickness of the rust film in the experiment, δ_F , and the effective oxygen diffusion coefficient came from the state of the numerical model when Equation (20) and the definition of $R_{ru l}$ are included. Two distinct ranges of values of the effective oxygen diffusion coefficient are identified in 5.21. The range expressed by the mean values of the effective diffusion coefficient of 1.73×10^{-9} m²/s was characteristic for the time of the experiments in which the rust film did not adjusted its structure (τ_f below 50 h and τ_d above 120 days). The range of values with D_{ef} around 0.29×10^{-10} m²/s corresponds to a much rigid (more compact) structure for oxygen diffusion to the reaction surface. The phenomenon of diffusion hardening of the rust film that we have identified can be supported by experimental analyses of the EDS and FTIR film that show, after tens and even hundreds of days, the change in its surface composition [30].

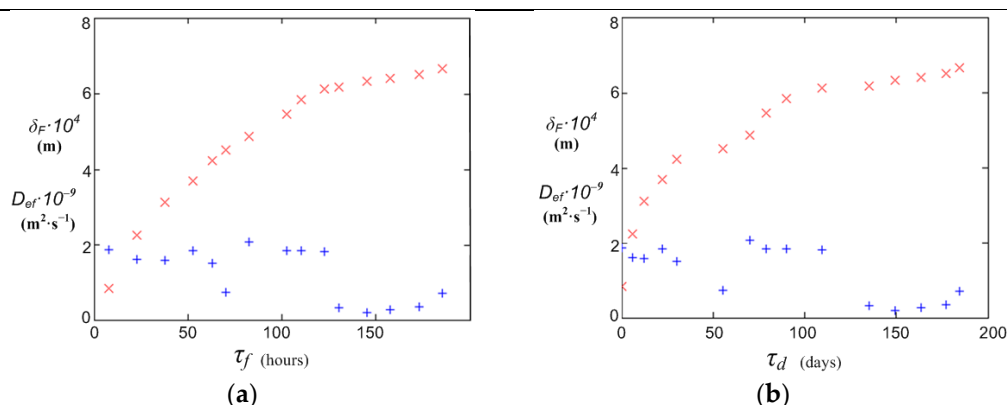


Figure 5.11 Rust film thickness and effective oxygen diffusion coefficient in terms of τ_f and τ_d : (a) hours; (b) days.

The values identified for the oxidation yield of Fe^{2+} on the steel plate were not influenced by the factors considered in Table 5.4. They can be characterized by the single value $\eta_{ox} = 0.167 \pm 0.012$. This result shows that iron oxidation occurs on the surface of the rust film where there is sufficient oxygen. Basically, the oxidation yield in film flow on a steel plate is, according to our measurements, in the range of 20–30 °C (Table 5.2). The same observation is valid for the values identified for the apparent constant of the surface reaction (k'_{rse}).

We further add in support of crust hardening that our investigation, which continued much longer than the times reported here, did not reveal surface rust removal by erosion due to the flowing film on the surface.

From subchapter 5.5 *Conclusions*, we note that the numerical transposition of the model allowed the identification of the model parameters, especially the apparent constant of the surface corrosion rate and the oxidation yield of Fe^{2+} released in corrosion. Considering the dynamics of the oxygen diffusion coefficient identified by the rust crust, it was found that, over time, the crust formed on the surface becomes increasingly resistant to oxygen diffusion, for which two distinct domains were identified.

Selective references:

1. https://www.meteoblue.com/ro/vreme/historyclimate/climatemodelled/constan%0c8%09ba_rom%0c3%0a2nia_680963
2. <https://www.google.com/search?q=texas+oil+terminals&oq=texas+oil+terminal&aqs=chrome.1.69i57j0i22i30l9.7985j0j7&sourceid=chrome&ie=UTF-8>
3. https://hdsc.nws.noaa.gov/pfds/pfds_map_cont.html?bkmrk=tx
4. Pierre R. Roberge, HANDBOOK OF CORROSION ENGINEERING, Third Edition, ISBN: 978-1-26-011696-0, McGraw-Hill Education, 2019
5. Acosta, G.; Veleva, L.; Chavez, L.; Lopez, J. Laminar Flow on the Corrosion Activity of A A6061-T6 in Seawater. *Metals* **2020**, *10*, 175.
6. Di Sarno, L.; Majidian, A.; Karagiannakis, G. The Effect of Atmospheric Corrosion on Steel Structures: A State-of-the-Art and Case-Study. *Buildings* **2021**, *11*, 571.
7. Wang, Z.; Wang, M.; Jiang, J.; Lan, X.; Wang, F.; Geng, Z. Atmospheric Corrosion Analysis of Rust Evolution Research of Q235 Carbon Steel at Different Exposure Stages in Chengdu Atmosphere Environment of China. *Scanning* **2020**, *2020*, 9591516.

CHAPTER 6

In chapter 6, most of the data in subchapter 6.3 were being published at the time of this thesis summary (under review), in *Metals*, Special Issue Corrosion Science and Engineering: Recent Research, Insights, and Challenges: Corrosion and Protection Marius Ciprian Ilie, Timur Vasile Chis, Ioana Maior, Cristian Eugen Raducanu *, Iuliana Mihaela Deleanu, Tanase Dobre* and Oana Cristina Parvulescu. *Experimental Investigation and Modeling. Considerations of Simultaneous Surface Steel Drops Evaporation and Corrosion. Metals*, 2023 (https://susy.mdpi.com/user/manuscripts/review_info/f7d37e9da6f8ace3d344e3c80e49d8f1)

Subchapter 6.1 presents generalities about droplet formation, presented as a phase change process, with a condensation mechanism that can lead to film condensation and droplet condensation, respectively. In the first case the thin condensation film on the condensation substrate acts as a barrier to heat transfer to the substrate [9]. In droplet condensation, the condensing substrate (surface) will be designed so that small droplets form and slide off when they reach a certain size, cleaning the surface and exposing it to fresh nucleation sites for further condensation [10]. In both mechanisms, even small amounts of non-condensable gas in the system determine the reduction of the heat transfer rate substantially [11-13] and cause the heat transfer to be associated with the mass transfer.

Subchapter 6.2 presents considerations regarding mass and heat transfer during droplet formation, and we note that the kinetics of heat transfer during condensation in droplets from moist air is characterized by the partial heat transfer coefficient for condensation, α very high, even 1000 W/(m² grd). It is also emphasized that for the heat transfer coefficient during condensation from air, it is considered to be expressed, in general, in the form of Equation (3), i.e. as a function of 4 factors $\Delta T_{sub}, UR, \theta_a, \beta$: (i) ΔT_{sub} – subcooling temperature, i.e. the temperature difference between the ambient environment and the condensation substrate; ii) UR – the water content of the surrounding atmosphere, i.e. humidity; iii) θ_a – the surface energy of the substrate, i.e. the droplet-solid contact angle; and iv) β – the substrate tilt angle, i.e. the angle between the condensation substrate and the gravitational field

$$\alpha = f(\Delta T_{sub}, UR, \theta_a, \beta) \quad (3)$$

Chapter 6.3. *Experimental Investigation of Multiple Droplet Corrosion on Plate* presents the results of the experimental study, submitted for publication in *Metals*, focused on the problem of steel surface corrosion as a kinetic expression when water droplets are repeatedly deposited and evaporated on/from its surface. We started from accepting the simplest corrosion model, according to which water forms a diffusion film through which oxygen will move towards the steel surface, where it reaches and determines the maintenance of anodic and cathodic processes, as a surface reaction [36]. The result of this model is in Equation (1) which shows the time dependence, expressed in years, of the corroded steel thickness (δ_{st}), which, as a convention, is given in μm . The experimentally determinable constants A and n take into account the influence of the factors mentioned above on this dynamics (A) as well as the superficial formation of the rust layer, which reduces the intensity of corrosion (n).

$$\delta_{st} = A \tau^n \quad (1)$$

This case of atmospheric corrosion can be characterized by approaches that consider it to be a case of simultaneous transfer of momentum and mass [39, 40], respectively of simultaneous transfer of heat and mass [41, 42], associated with the electrochemical corrosion process that occurs on the surface. In the case of droplet corrosion, their appearance on the condensing surface is a relatively fast process, under 10-15 minutes [43], if the condensing conditions are met [44], as shown by Equation (2) where p_s is the pressure of water saturation, t_s and t_g are the surface temperature and air temperature respectively, U_r gives the relative air humidity and t_r is the dew point temperature.

$$p_s(t_s) \leq p_s(t_g)U_r \text{ or } t_s \leq t_r(U_r) \quad (2)$$

Considering these remarks, we focused in this paper on the analysis of kinetics in the corrosion process of the droplets upon their evaporation. Many of the current approaches to modeling droplet corrosion refer to the Evans droplet model [42, 45, 46] which in its current form [46] characterizes the onset of hemispherical droplet corrosion using unsteady-state species concentration field equations with reactions of surface at the cathodic and anodic (droplet-based) sites. For small hemispherical drops, the absence of movement in the droplet can be accepted [46], while for large drops this fact is no longer acceptable because here the evaporation of the droplet is accompanied by the Marangoni effect [48-50]. For small droplet corrosion, the COMSOL solution of the Evans model [47], where it uses only an anodic site on the surface and

a cathodic site near the droplet hemisphere, shows both that the current density curves in the droplet inside are arcs, starting from the anode and closing at the cathodic site, and that, here, in the cathodic site (the area where the drop closes to the surface), the concentration of dissolved species reaches maximum values.

Subchapter 6.3.2 described the method and the experimental installation (Fig. 6.1)

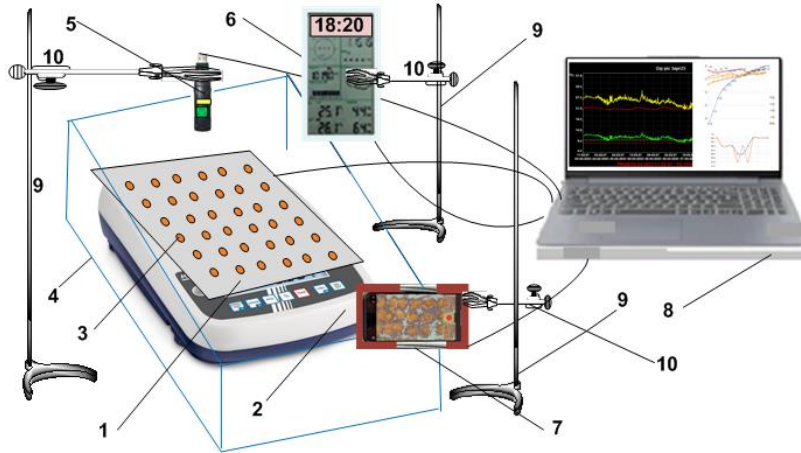
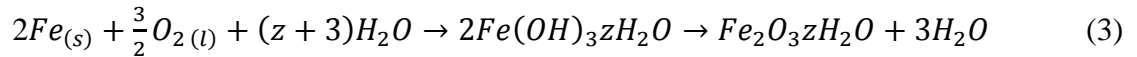


Figure 6.1. Experimental laboratory setup for corrosion in water droplets: (1) black steel plate for corrosion tests; (2) precision balance; (3) water droplets to corrode; (4) balance protection enclosure; (5) temperature humidity dew point Data Logger; (6) laboratory meteorological micro station; (7) filming device; (8) data registration and processing system; (9) stands; (10) clamps stand.

The corrosion processes from one drop, complemented with total Fe^{+2} to Fe^{+3} oxidation and with metal oxide precipitation, is expressed [38-40] by Equation (3):



In subchapter 6.3.3. *Mathematical modeling*, three possible models were presented for the evolution of the droplet shape in the evaporation process (Fig. 6.2).

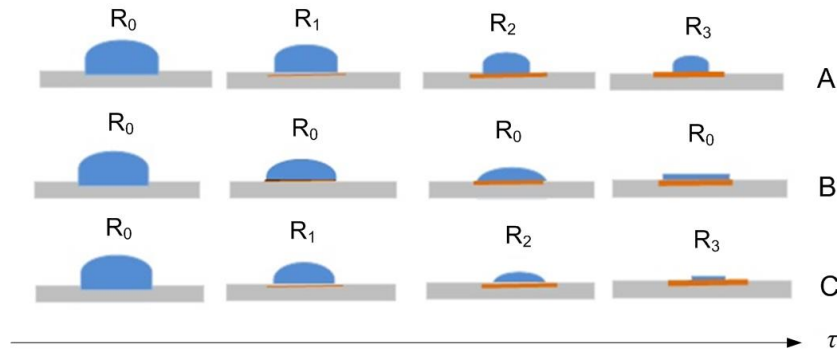


Figure 6.2. Possible models for the evolution of droplets shape during their evaporation, hemisphere shape: (A) descending hemisphere; (B) spherical cap with trace preservation; (C) spherical cap without trace preservation; rust as brown color.

Regardless of the shape, if it is identifiable, as shown in Figure 6.3, then its analytical expression ($y = f(x)$, $x = \varphi(y)$) becomes possible from the knowledge of the instantaneous volume [53] as shown by Equation (6). The surface produced by rotating $y = f(x)$, $x = \varphi(y)$ with respect to the x and y axes respectively [53] is the surface of the air drop interphase (Equation (7)).

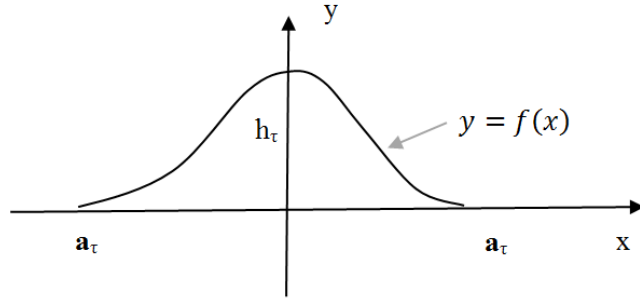


Figure 6.3. Droplet shape in y - x graphic representation

$$V_{\tau 0x} = \pi \int_{-a_\tau}^{a_\tau} (f(x))^2 dx \quad V_{\tau 0y} = \pi \int_0^{h_\tau} (\varphi(y))^2 dy \quad (6)$$

Our observations, justified with the presentation of the results, support that for an evaporation of droplets on a steel surface the initial shape and its evolution correspond to a paraboloid (Equation (8)). Here R is the initial radius of the droplet, deposited on the surface, and h_τ shows the distance from the center of the droplet to its boundary.

$$\frac{x^2}{R^2} + \frac{y^2}{h^2} - 1 = 0 \quad (8)$$

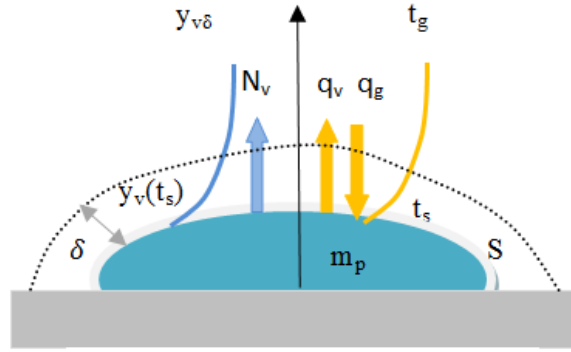


Figure 6.4. Representation of mass and heat transfer when evaporating the droplet from the steel surface

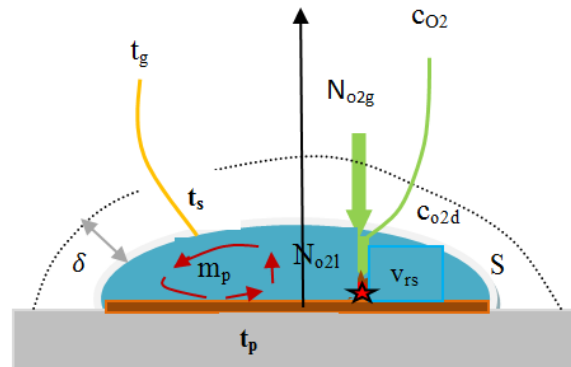


Figure 6.5. The process of oxygen transfer and corrosion inside the droplet with Marangoni flow

The assumption that the droplet evaporates keeping its original trail allowed the analysis by modeling the two processes in the droplet. Thus, Figure 6.4 shows the simultaneous phenomenology of mass and heat transfer during droplet evaporation. Figure 5 shows the transfer of O_2 inside the droplet and its consumption, through the reaction on the surface, with the generation of rust. We mention that in the droplet inside there is an internal flow determined by the association of the Marangoni phenomenon with its evaporation [54-56]. Figure 6.5 schematically represents this flow. When falling outside, over the boundary layer, the experimental conditions characterize an environment or at most in natural convection. Under these conditions, the vapors leaving the surface of the drop pass, by diffusion over the inert (air), through the boundary layer of thickness δ . On any direction z , normal to the surface of the drop,

their specific flow rate is given by the differential expression in Equation (9), where c is the total molar concentration and D_v represents the air vapor diffusion coefficient.

$$N_v = -\frac{cD_v}{(1-y_v)} \frac{dy_v}{dz} \quad (9)$$

Figure 6.4 shows the vapor mole fraction at the droplet surface and outside the boundary layer, so that the integration of Equation (9) gives the integral expression of the vapor flow (Equation (10)).

$$N_v = \frac{cD_v}{\delta y_{Bm}} (y_v(t_s) - y_{v\delta}) \quad (10)$$

Equation (11) is written to highlight the driving force and the mass transfer coefficient, in the form (12). Since c , D_v , δ and even y_{Bm} in (10) depend on t_g and t_s or more correctly on those differences, it was considered for k_g as dependent on the heat transfer driving force $t_g - t_s$. So:

$$k_g = \frac{D_v}{\delta y_{Bm}} = k_g(t_g - t_s) \quad (11)$$

$$N_v = ck_g(t_g - t_s)(y_v(t_s) - y_{v\delta}) \quad (12)$$

A balance for the duration from τ to $\tau + d\tau$, when denoting the interphase transfer surface (evaporation surface) $S(\tau)$, yields Equation (12). Here $S(\tau)$ depends on the instantaneous mass of the droplet (m_p) as follows from the coupling of Equations (6), (7) and (8), where we put $V_{\tau\theta y} = m_{p\tau}/\rho_a$. With this consideration, Equation (13) can be written as Equation (14).

$$\frac{dm_p}{d\tau} = N_v M_w S(\tau) \quad (13)$$

$$\frac{dm_p}{d\tau} = \alpha f(m_p) N_v M_w \quad (14)$$

If we had expressions or values for the mass transfer coefficient, for the interface temperature as well as for the function $f(m_p)$, then the momentary mass of the droplet becomes analytically expressible. Table 3 shows the calculation of the transfer surface, for the droplet masses of interest in the present work, so that α and $f(m)$ from Equation (14) can be identified.

Table 6.3. Calculation of droplet evaporation surface value as a function of droplet mass for the case of paraboloid cap with constant cap radius

Parameters	Surface values as function of droplet mass						
R (cm)	0.30						
m_p (g)	0.060	0.050	0.040	0.030	0.020	0.010	0.005
h or h_r (cm)	0.312	0.276	0.235	0.183	0.133	0.069	0.035
S or $S(\tau)$ (cm ²)	0.588	0.528	0.453	0.378	0.286	0.283	0.283
$\alpha f(m_p)$	$\alpha = \pi R^2$ $f(m_p) = 0.908 + 7.08m_p + 221.2 m_p^2$						
R (cm)	0.35						
m_p (g)	0.060	0.050	0.040	0.030	0.020	0.010	0.005
h or h_r (cm)	0.252	0.228	0.189	0.147	0.101	0.052	0.022
S or $S(\tau)$ (cm ²)	0.595	0.530	0.458	0.385	0.385	0.385	0.385
$\alpha f(m_p)$	$\alpha = \pi R^2$ $f(m_p) = 1.037 - 7.79m_p + 277.5 m_p^2$						
R (cm)	0.40						
m_p (g)	0.060	0.050	0.040	0.030	0.020	0.010	0.005
h or h_r (cm)	0.217	0.185	0.152	0.116	0.078	0.040	0.020
S or $S(\tau)$ (cm ²)	0.601	0.529	0.505	0.503	0.503	0.503	0.503
$\alpha f(m_p)$	$\alpha = \pi R^2$ $f(m_p) = 1.043 - 5.98m_p + 135.7 m_p^2$						
R (cm)	0.45						
m_p (g)	0.060	0.050	0.040	0.030	0.020	0.010	0.005
h or h_r (cm)	0.179	0.157	0.123	0.093	0.062	0.031	0.016
S or $S(\tau)$ (cm ²)	0.666	0.656	0.642	0.636	0.636	0.636	0.636
$\alpha f(m_p)$	$\alpha = \pi R^2$ $f(m_p) = 1.005 - 0.933m_p + 27.5 m_p^2$						

To be functional, the model, in terms of the mass dynamics of the evaporating water droplet at the surface, needs a solution to calculate the surface temperature of the water droplet and also to account for the mass transfer coefficient from droplet to the surrounding air.

In this sense, if the heating of the droplet is neglected, then the temperature t_s results from the fact that the specific heat flow brought by convection to the droplet (Equation (15)) is equal to the specific heat flow due to vaporization (Equation (16)). It is identified in Equation (15) that the value of the heat transfer coefficient is a function of the air temperature difference and the surface drop. So $\alpha_g = \alpha_g(t_g - t_s)$. In Equation (16) the latent heat of vaporization of water was denoted by r_v .

$$q_g = \alpha_g(t_g - t_s) = \alpha_g(t_g - t_s)(t_g - t_s) \quad (15)$$

$$q_v = N_v M_w r_v \quad (16)$$

The mention equality of q_g and q_v , coupled with N_v relationship, goes for t_s in Equation (17).

$$\alpha_g(t_g - t_s)(t_g - t_s) = c k_g(t_g - t_s)(y_v(t_s) - y_{v\delta}) M_w r_v \quad (17)$$

The transfer of mass and heat respectively from and to the droplet occurs through the boundary layer of the droplet, as shown in Figure 4. Thus, the analogy of transfer phenomena [57, 58] can be used to express $k_g(t_g - t_s)$ using $\alpha_g(t_g - t_s)$. This is given by Equation (18), where ρ_g is the air density and c_{pg} represents its specific heat coefficient. Coupling Equation (18) with Equation (19) leads to the expression of the droplet surface temperature by the conditional Equation (19). For $y_v(t_s)$ the Equation (20) is used, where p is the air pressure and A, B, C are the Antoine constants for expressing the water saturation vapor pressure.

$$k_g(t_g - t_s) = \frac{\alpha_g(t_g - t_s)}{\rho_g c_{pg}} \quad (18)$$

$$t_s = t_g - \frac{c}{\rho_g c_{pg}} (y_v(t_s) - y_{v\delta}) M_w r_v, \quad y_v(t_s) > y_{v\delta} \quad (19)$$

$$y_v(t_s) = \frac{10^{\frac{A - B}{t_s + C}}}{p} \quad (20)$$

Regarding Equation (19), it should be specified that $y_{v\delta}$ depends on the relative air humidity (φ) and the saturation pressure of water vapor at its temperature t_g . It should also be said that, after t_s , this relationship is a transcendent equation, so to analytically or graphically raise the dependence $t_s = t_s(\varphi, t_g)$ a calculation program is required.

To complete the model of droplet evaporation by natural convection, i.e. the model showing how the droplet mass evolves over time as a function of initial radius, shape, air relative humidity and air temperature, a relation expressing values of the heat transfer coefficient for this heat transfer mechanism is needed. A relation from the literature [59, 60] was thus chosen, here specified in the form of Equation (21), where the coefficients a, m and l_c have the specifications in Table 6.4.

$$\alpha_g = \alpha_g(t_g - t_s) = a \left(\frac{t_g - t_s}{l_c} \right)^m \quad (21)$$

Table 6.4. Values for the parameters of Equation (21)

N.C.	Parameter	Vertical surface	Horizontal upper surface	Horizontal lower surface
1	a	1.420	1.320	1.520
2	m	0.250	0.250	0.330
3	l_c	0.112	0.055	0.055

For the modeling of the corrosion process of the droplet-steel interface, it is considered to progress more slowly than the evaporation process. The Equation (22) expresses the specific flow rate of oxygen. This becomes (23) by expressing c_{O_2s} from the equality of oxygen transferred with oxygen consumed by the reaction surface.

$$N_{O2l} = N_{O2} = k_l(c_{O2d} - c_{O2s}) \quad (22)$$

$$N_{O2l} = \frac{k_l k_{rsa}}{k_l + k_{rsa}} c_{O2d} \quad (23)$$

In Equation (23) c_{O2d} can be considered as the equilibrium concentration of oxygen at the droplet surface temperature. The mass transfer coefficient k_l , given by adapting the literature [61, 62], takes into account the fact that the driving force for the Marangoni flow in the droplet inside is represented by the surface tension difference of the water at the droplet surface, $\sigma(t_s)$, and at the solid surface, ($\sigma(t_p) \approx \sigma(t_g)$), as shown by Equation (24). For the apparent reaction constant, k_{rsa} , Equation (25) [40] was considered. Here the value of 2.3×10^{-5} m/s [9] was assumed for k_{rs} (oxygen surface reaction constant when the steel surface is not rusted (new and this is a novelty regarding the model from [40] previously)). In regard to the surface reaction rate constant, we show that it has a rather complex meaning. Thus, seeing the corrosion process as a process with a chemical kinetics in which the solid reacts with the limiting reactant (oxygen in water in the case of pure corrosion), then it is influenced by local surface structure issues (local crystallinity, intra-granular inclusions). As these structural irregularities are distributed, the surface is seen with average properties. As a result, the reaction rate constant on the surface corrosion process refers to a surface seen with averaging of unevenness. The rust thickness δ_r is linearly dependent on the mass of rust deposited at the solid interface of the droplet (Equation (26)). For the oxygen diffusion coefficient through the rust layer, the range of values is $0.2 \times 10^{-9} - 2 \times 10^{-9}$ m²/s [40]

$$k_l = a \frac{\sigma(t_g) - \sigma(t_s)}{\eta} = 3.75 \times 10^{-5} \frac{\sigma(t_g) - \sigma(t_s)}{\eta} \quad (24)$$

$$\frac{1}{k_{rsa}} = \frac{1}{k_{rs}} + \frac{\delta_r}{D_{O2ef}} \quad (25)$$

$$\delta_r = \frac{m_{ru}}{\pi R_0^2 \rho_{ru}} \quad (26)$$

The momentary flow rate of consumed oxygen is given by Equation (27) where $S(\tau)$ can be expressed as shown in Table 1. Based on Equation (3), the mass of iron dissolved under the droplet (Equation (28)) is obtained, respectively the mass of deposited rust under the droplet and on the contour of its trail (Equation (28)). As shown above, the rust mass was measured for each experimental test. Its dynamics, resulting from the measurements performed, can be used to validate the developed models, as well as to promote a global kinetic relationship of droplet corrosion, as shown by Equation (1).

$$\frac{dm_{O2}}{d\tau} = S(\tau) N_{O2l} M_{O2} = \alpha f(m_p) N_{O2l} M_{O2}, \quad \tau = 0 \quad m_{O2} = 0 \quad (27)$$

$$m_{Fe} = \frac{4}{3} m_{O2} \frac{M_{Fe}}{M_{O2}} \quad (28)$$

$$m_{ru} = \frac{2}{3} m_{O2} \frac{M_{ru}}{M_{O2}} \quad (29)$$

In subchapter 6.3.4. *Results*, it was shown that the experimental investigation followed the simultaneous process of droplet evaporation and steel corrosion, evaluating in this sense: i) the dynamics of the water mass of the drops located (deposited) on the plate; ii) the state of the form of the evaporating droplets; iii) air parameters near the plate with evaporating droplets and iv) increase in plate mass due to rust deposition from the corrosion process.

The diameter of the shape was found to be between 5 and 10% larger than that of the droplet.

Both Figure 6.7 and Figure 6.8 come to support that, during evaporation, the droplet shrinks while keeping its diameter very close, practically the same, to the original diameter of the droplet. It is stated that in Table 6.3 in the building of functions $f(m_p)$ this fact, now supported experimentally, was used, namely that the drop shrinks while keeping its initial diameter.

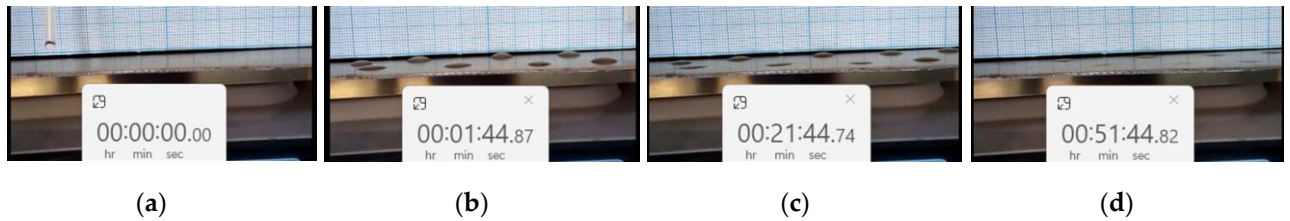


Figure 6.7. Frames from droplet evaporation-corrosion on a steel surface in Test 1, showing that droplet shrinkage occurs with droplet diameter maintained: ($\phi = 36.5\%$, $d_0 = 7.2$ mm): (a) blank black steel plate, starting droplets deposition; (b) droplet already in position; (c) evaporation evolution after 21 min; (d) ending of evaporation and shape formation; (d) bottom - the third deposition of the drop, $\phi = 43.5\%$, $d_0 = 7.2$ mm)

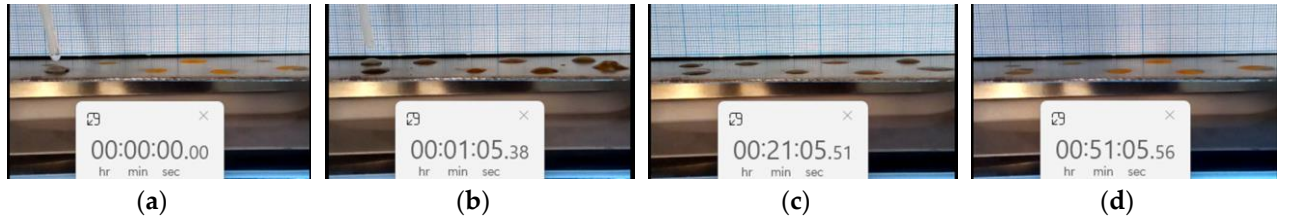


Figure 6.8. Frames from droplet evaporation-corrosion on a steel surface in Test 3, showing that droplet shrinkage occurs with droplet diameter maintained: ($\phi = 43.5\%$, $d_0 = 7.2$ mm): (a) starting droplets deposition onto rusted old trails; (b) droplet already in position; (c) evaporation evolution after 21 min; (d) ending of evaporation with the new layered rust

Tables 6.5-6.8 and Figures 6.9-6.12 present primary data for four evaporation-corrosion tests when the plate surface is of steel, with its composition shown in Table 6.1. It is noted that the presence of *NaCl* in the corrosion medium (column F from Table 6.7 and Table 6.8 compared to the same column from Tables 6.4 and Table 6.5) significantly changes the mass of rust obtained at the end of the test.

Table 6.5. Experimental data characterizing the evaporation of droplets from the steel surface and its corrosion (Test 1, $d_0 = 7.78 \pm 0.31$ mm, $d_u = 8.05 \pm 0.45$ mm)

A	B	C	D	E	F	G	H	I	J	K	L	M
1	0		487.25	0.00		27.7	53.9	17.5				0.0
2	30		486.35	0.90		27.8	52.9	17.3				0.5
3	60		485.30	1.05		27.9	53.3	17.5				1.0
4	90	482.15	484.00	1.30		27.9	52.8	17.3				1.5
5	120		483.50	0.50	0.05	28.0	52.1	17.2	26.0	55.0	757.6	2.0
6	150		482.80	0.70		27.8	52.8	17.2				2.5
7	180		482.20	0.60		27.8	52.9	17.3				3.0
8	210		482.20	0.00		27.8	53.2	17.3				3.5

(A) current number; (B) time (min); (C) initial plate mass (g); (D) current plate mass (g); (E) evaporated water (g); (F) resulted rust mass (g); (G) air temperature ($^{\circ}\text{C}$); (H) air humidity (%); (I) dew point temperature ($^{\circ}\text{C}$); (J) external air temperature($^{\circ}\text{C}$); (K) external air humidity (%); (L) air environment pressure (mmHg); (M) cumulated time (h).

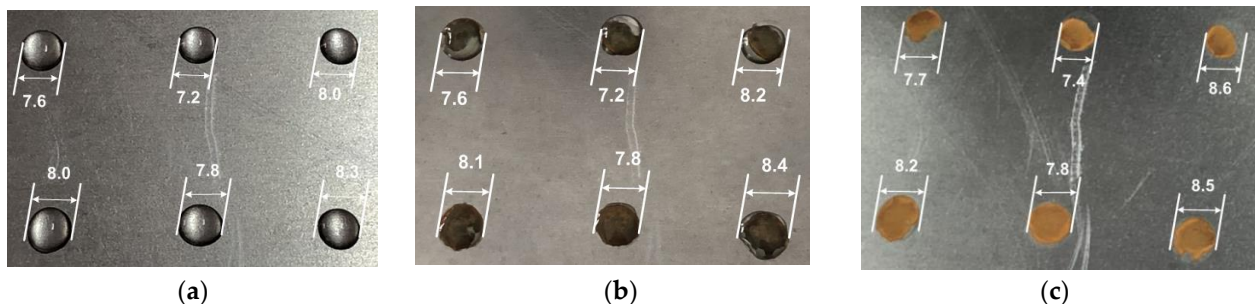


Figure 6.9. Droplets shape and diameter during their evaporation from the steel surface in evaporation - corrosion Test 1: (a) initial; (b) after 120 min; (c) after 210 min (end of test). Mean diameter and standard deviation are shown in Table 6.5.

SUMMARY

The chlorine and sodium ions presence in drops, in this case at a concentration level of 1g/L NaCl, does not change the dynamics of evaporation instead, as previously mentioned, it causes the increasing of corrosion specific flow rate from 0.01 - 0.012 mg_{Fe}·cm⁻²·h⁻¹ (Table 6.5 and Table 6.6, column F) to 0.05 - 0.06 mg_{Fe}·cm⁻²·h⁻¹ (Table 6.7 and Table 6.8, column F).

Table 6.6 Experimental data characterizing the evaporation of droplets from the steel surface and its corrosion (Test 4, $d_0 = 7.79 \pm 0.54$ mm, $d_u = 8.38 \pm 0.55$ mm)

A	B	C	D	E	F	G	H	I	J	K	L	M
1	0		486.85	0.00		27.2	43.2	13.6				81.0
2	30		484.35	2.50		27.4	42.8	13.6				81.5
3	60	482.30	484.10	0.25	0.05	27.5	42.5	13.6	2.0	44.0	756	82.0
4	90		482.80	1.30		27.7	41.9	13.5				82.5
5	120		482.35	0.00		27.9	40.9	13.3				83.0
6	150		482.35	0.00		27.8	40.9	13.3				83.5

(A) current number; (B) time (min); (C) initial plate mass (g); (D) current plate mass (g); (E) evaporated water (g); (F) resulted rust mass (g); (G) air temperature (C°); (H) air humidity (%); (I) dew point temperature (C°); (J) external air temperature(C°); (K) external air humidity (%); (L) air environment pressure (mmHg); (M) cumulated time (h).

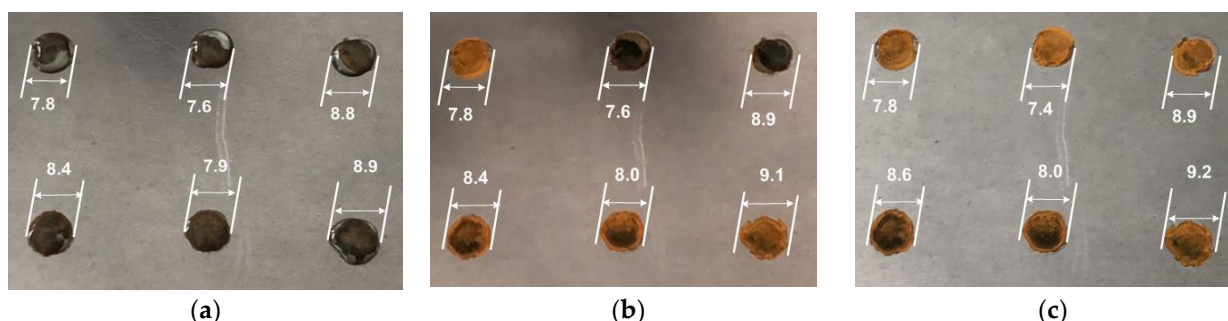


Figure 6.10. Droplets shape and diameter during their evaporation from the steel surface in evaporation - corrosion Test 4: (a) initial; (b) after 120 min; (c) after 210 min (end of test). Mean diameter and standard deviation are shown in Table 6.6

Table 6.7. Experimental data characterizing the evaporation of droplets from the steel surface and its corrosion (Test 28, $d_0 = 8.70 \pm 0.44$ mm, $d_u = 8.93 \pm 0.50$ mm)

A	B	C	D	E	F	G	H	I	J	K	L	M
1	0		501.60	0.00		28.5	32.2	10.3				9711.5
2	30		498.00	3.60		28.3	31.7	9.8				9712.0
3	60		497.30	0.70		28.2	33.4	10.5				9712.5
4	90		495.40	1.90		28.3	32.6	10.3				9713.0
5	120		492.35	3.05		28.1	32.2	9.9				9713.5
6	150	484.45	490.20	2.15	0.25	28.1	32.1	9.9	32	45	759	9714.0
7	180		488.40	1.80		28.0	31.7	9.6				9714.5
8	210		487.65	0.75		28.0	31.8	9.6				9715.0
9	240		486.30	1.35		27.9	32.4	9.8				9715.5
10	270		485.40	0.90		27.8	33.1	10.1				9716.0
11	300		484.85	0.55		27.7	33.6	10.2				9716.5
12	330		484.85	0.00		27.6	34.1	10.3				9717.0

(A) current number; (B) time (min); (C) initial plate mass (g); (D) current plate mass (g); (E) evaporated water (g); (F) resulted rust mass (g); (G) air temperature (C°); (H) air humidity (%); (I) dew point temperature (C°); (J) external air temperature(C°); (K) external air humidity (%); (L) air environment pressure (mmHg); (M) cumulated time (h).

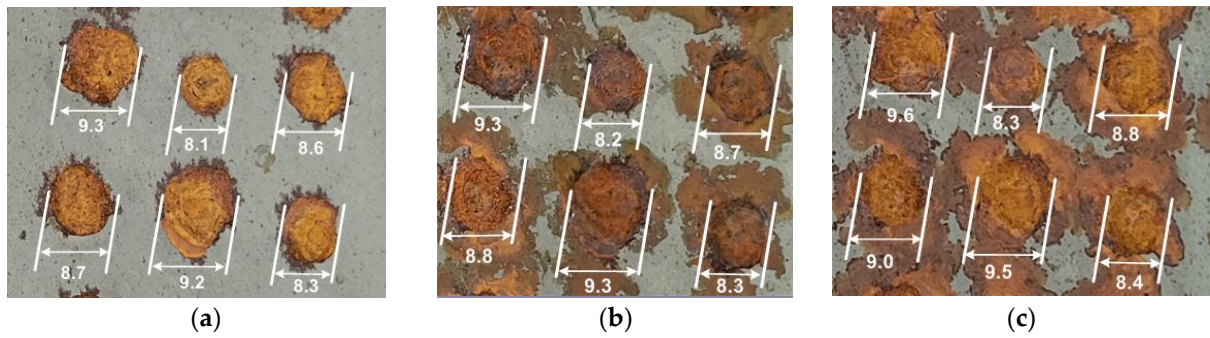


Figure 6.11. Droplet shape and diameter during their evaporation from the steel surface in the evaporation - corrosion test 28: (a) initial; (b) after 120 min; (c) after 330 min (end of test). Mean diameter and standard deviation are shown in Table 6.7)

Table 6. 8. Experimental data characterizing the evaporation of droplets from the steel surface and its corrosion (Test 30, $d_o = 9.05 \pm 0.47$ mm, $d_u = 9.32 \pm 0.49$ mm)

A	B	C	D	E	F	G	H	I	J	K	L	M
1	0		496.15	0.00		28.9	37.8	13				9769.0
2	30		493.10	3.05		29.1	37.6	13.1				9769.5
3	60		491.20	1.90		29.2	37.7	13.3				9770.0
4	90	485.20	489.35	1.85	0.30	29.0	36.9	12.7	30	35	757	9770.5
5	120		488.15	1.20		28.8	37.1	12.7				9771.0
6	150		486.70	1.45		28.7	37.1	12.6				9771.5
7	180		485.50	1.20		28.6	37.1	12.5				9772.0
8	210		485.50	0.00		28.5	36.7	12.2				9772.5

(A) current number; (B) time (min); (C) initial plate mass (g); (D) current plate mass (g); (E) evaporated water (g); (F) resulted rust mass (g); (G) air temperature (C°); (H) air humidity (%); (I) dew point temperature (C°); (J) external air temperature(C°); (K) external air humidity (%); (L) air environment pressure (mmHg); (M) cumulated time (h).

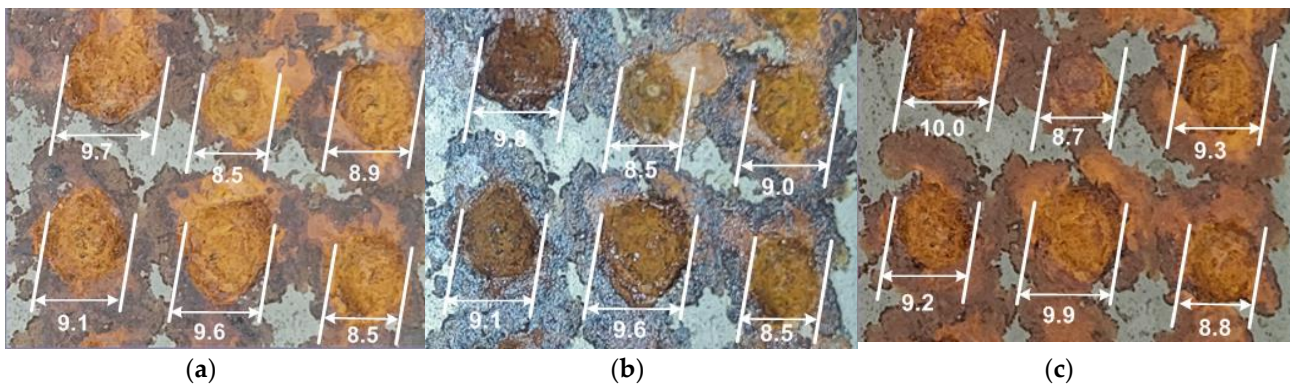


Figure 6.12. Droplets shape and diameter during their evaporation from the steel surface in the fourth evaporation - corrosion test 30: (a) initial; (b) after 120 min; (c) after 210 min (end of test). Mean diameter and standard deviation are shown in Table 6.8)

These tables and figures (each of them) contain all the necessary data (evaporated water, respectively deposited rust mass as dynamics referable to a single droplet) so that they can be used in testing the developed model.

In subchapter 6.3.5 *Discussions* it was showed that the model testing involved the calibration and numerical transposition of the model.

Mean values for relative humidity (t_g) and air temperature (t_g) near the plate were used for calibration. The values identified for the surface reaction rate constant (k_{rs}) and for the effective oxygen diffusion coefficient through the rust layer (D_{O2ef}) are consistent with those from film corrosion [40], when evaporation-corrosion occurs in droplets of the water. The higher values of the corrosion rate constant k_{rsin} by $NaCl$ solution droplets show the intensification of the anodic reaction on the steel surface, as reported in other works [63, 64]. The high value of D_{O2efin} in this case indicates a rather permeable structure of the rust formed in the corrosion process, as well as that here the transport of oxygen is facilitated by the action of Cl^- ions. For the constant α in

Equation (24) the model performed well with a higher value compared to those found in the literature (3.75×10^{-5}). The numerical transposition of the model had the microsequences: a) the choice of parameters: coefficient α and power m in relation (21), coefficient a from Equation (24), k_{rs} and respectively the relation D_{O2efin} (Equation (25)); b) selection of tests for corrosion with drops containing $NaCl$; c) setting an option such as relative humidity and temperature to be taken as a function of time or as mean values; d) the effective expression of the numerical model for the dynamics of the mass of the drop, respectively the dynamics of the mass of rust deposited under the drop;

Table 6.9 summarizes the model calibration results.

Table 6.9. Values of some model parameters and strategy from Equation (21)

C.N.	Case	Data	φ	t_g	k_{rs} (Eq.25)	D_{O2ef} (Eq.23)	a (Eq.21)	m (Eq.21)	α (Eq.24)
1	Water droplet	Tabel 6.5	mean	mean	4.5×10^{-5}	9.1×10^{-10}	$f(\varphi, t_g)$	0.33	2.63×10^{-4}
		Tabel 6.6			(m/s)	(m^2/s)			($m^2 \cdot s$)
2	Water droplet	Tabel 6.8	mean	mean	9.5×10^{-4}	5.1×10^{-9}	$f(\varphi, t_g)$	0.33	2.63×10^{-4}
	with $NaCl$				(m/s)	(m^2/s)			($m^2 \cdot s$)

If to the presentation of Equation (21) it is added that in addition to heat transport by natural convection we have an additional heat transport by vapors leaving the surface, then the value chosen for the constant m is supported as well as the fact that a can be a function of φ and t_g ($a = f(\varphi, t_g)$).

The result of these simulations is concentrated in Figures 16.3-6.17 and Table 6.10, which characterizes, in comparison with those specified above, each individual test.

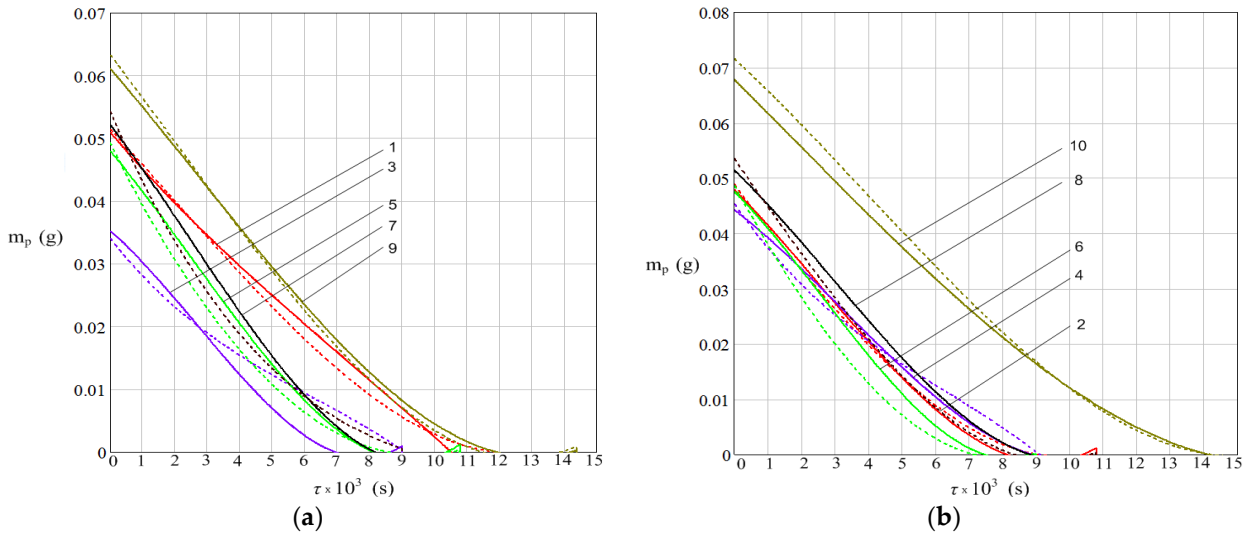


Figure 6.13. Dynamics of droplets mass during their evaporation for tests 1 to 10 ($T_1 \dots T_{10}$): (a) T_1 – red; T_3 – blue; T_5 – green; T_7 – black; T_9 – brown; (b) T_2 – red; T_4 – blue; T_6 – green; T_8 – black; T_{10} – brown; Continuous curves – model, dashed curves – experimental

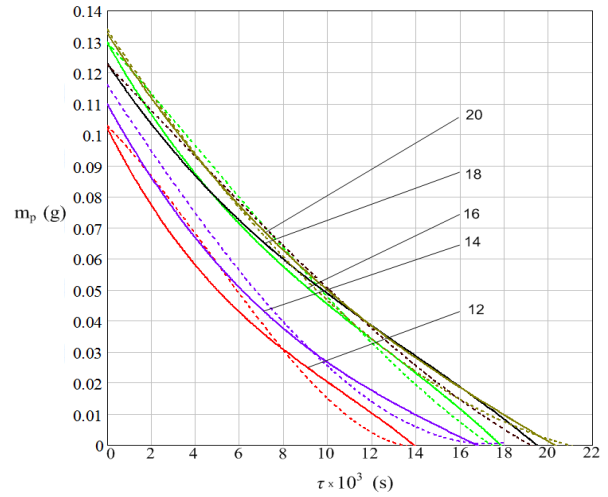
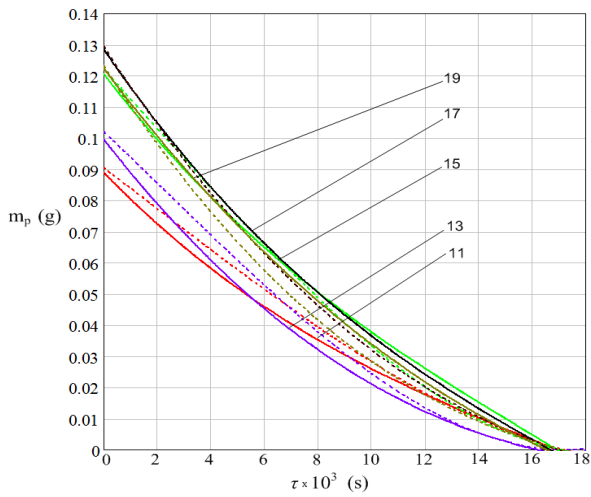


Figure 6.14. Dynamics of droplets mass during their evaporation for tests 11 to 20 ($T_{11} \dots T_{20}$): (a) T_{11} – red; T_{13} – blue; T_{15} – green; T_{17} – black; T_{19} – brown; (b) T_{12} – red; T_{14} – blue; T_{16} – green; T_{18} – black; T_{20} – brown; Continuous curves – model, dashed curves – experimental

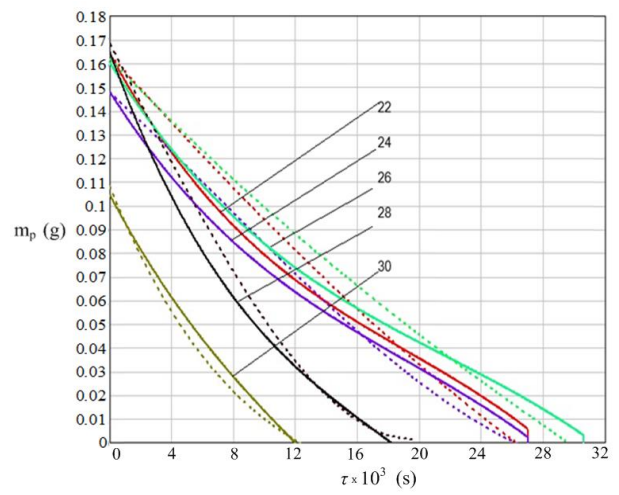
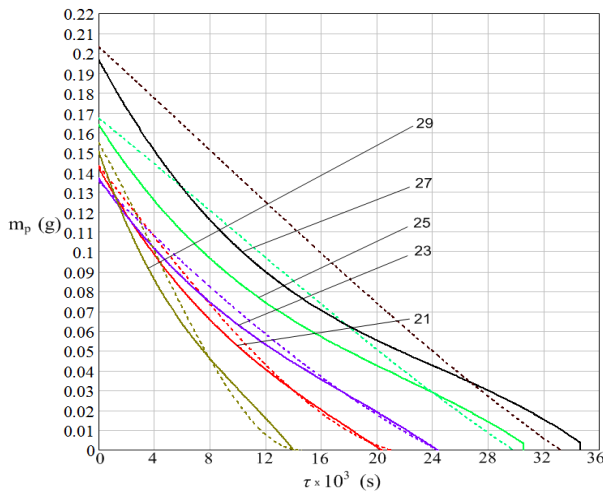


Figure 6.15. Dynamics of droplets mass during their evaporation for tests 21 to 30 ($T_{21} \dots T_{30}$): (a) T_{21} – red; T_{23} – blue; T_{25} – green; T_{27} – black; T_{29} – brown; (b) T_{22} – red; T_{24} – blue; T_{26} – green; T_{28} – black; T_{30} – brown; Continuous curves – model, dashed curves – experimental

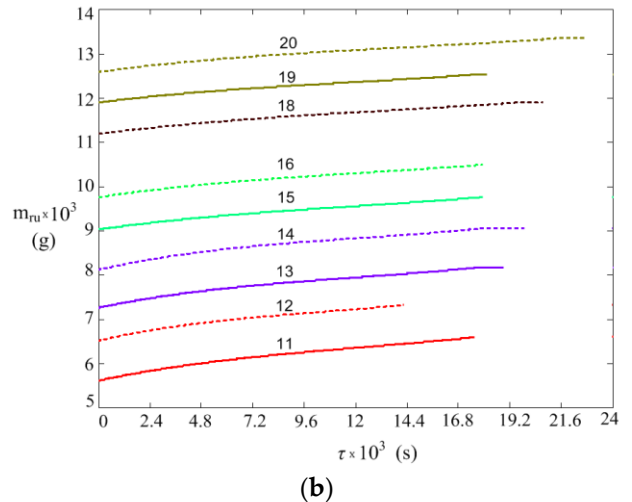
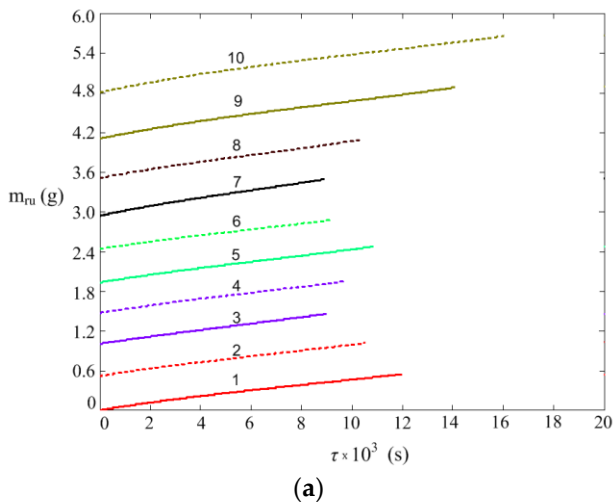


Figure 6.16. Dynamics of deposited rust mass during droplets evaporation-corrosion, from one droplet, experimental for tests $T_1 \dots T_{20}$: (a) T_1 to T_{10} ; (b) T_{11} to T_{20} ; Continuous curves - model, dashed curves - experimental

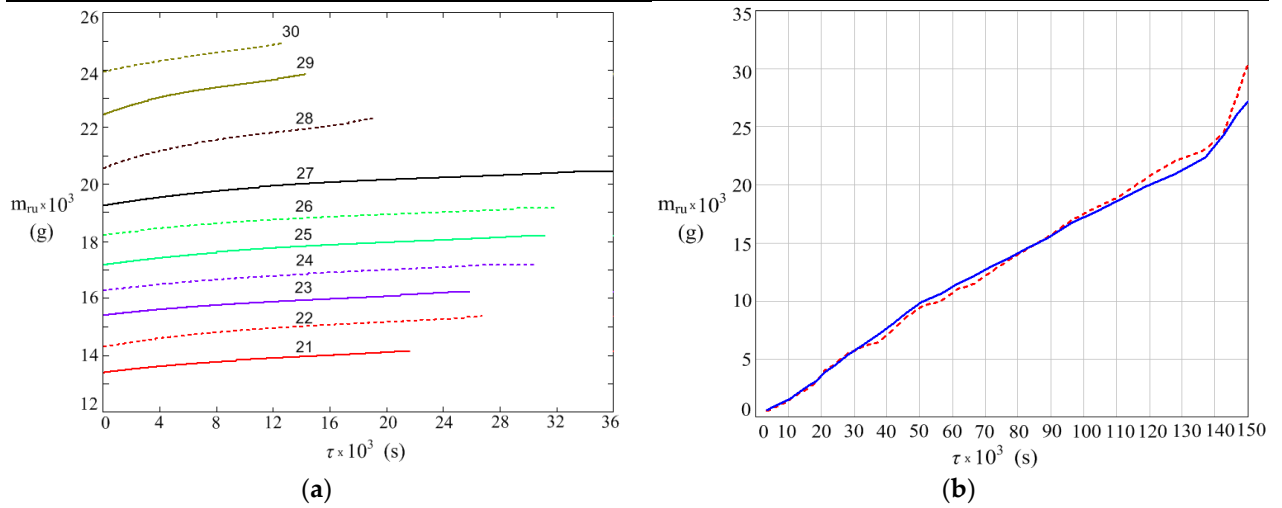


Figure 6.17. Dynamics of deposited rust mass during droplets evaporation – corrosion: (a) in experimental tests T1₂₁...T₃₀; (b) cumulated mass rust vs. effective corrosion time; line - model, dashed line - experimental)

The relative deviation between the experimental values and those according to the model, presented in Table 6.10 for the dynamics of the droplet mass, respectively for the dynamics of the deposited rust mass, it is stated that it was calculated according to the available data, as it appears from the Equation (30) and (31) respectively. In Equation (30) n_i is the number of time steps since model integration for the i evaporation-corrosion test.

$$\varepsilon_{mpMi} = \frac{1}{n_i} \frac{\sum_{j=1}^{n_i} m_{pex}(\tau_j) - \sum_{j=1}^{n_i} m_{pt}(\tau_j)}{\sum_{j=1}^{n_i} m_{pex}(\tau_j)} 100 \quad i = 1, 2 \dots 30 \quad (30)$$

$$\varepsilon_{mruMi} = \frac{m_{ruexi} - m_{ruti}}{m_{ruexi}} 100 \quad i = 1, 2 \dots 30 \quad (31)$$

Table 6.10. Corrosion tests and comparison of experimental results with those according to the model by relative deviations (ε_{mpM} , ε_{mruM})

Test	m_{p0} (g)	φ (l)	t_g (°C)	a (20)	ε_{mpM} (%)	ε_{mruM} (%)	τ_t (h)	τ_c (h)	τ_p (h)
1	0.0500	0.531	27.8	7.66	-8,14	-9.31	3.5	3.5	3.5
2	0.0480	0.454	28.2	7.69	-7.65	-2.85	3.0	6.5	30.5
3	0.0360	0.354	28.3	5.18	11.31	2.94	2.5	9.0	57.5
4	0.0455	0.427	27.6	5.95	18.62	1.94	2.5	11.5	83.5
5	0.0490	0.328	27.7	5.23	15.18	4.39	3.0	14.5	134
6	0.0480	0.306	27.4	5.41	-11.50	15.55	2.5	17.0	161
7	0.0535	0.312	28.2	5.33	14.14	8.65	2.5	19.5	187
8	0.0535	0.350	28.9	5.19	0.717	11.02	3.0	22.5	214
9	0.0630	0.383	25.6	5.41	15.29	5.62	4.0	26.5	1658
10	0.0700	0.339	26.3	4.39	1.81	-161	4.5	31.0	1687
11	0.0915	0.479	21.4	6.80	8.45	2.35	5.0	36.0	2892
12	0.1040	0.441	21,5	7.16	-12.74	3.83	4.0	40.0	2920
13	0.1020	0.301	24.9	4.39	18.00	4.79	5.0	45.0	5517
14	0.1150	0.261	25.4	3.79	-0.96	2.45	5.0	50.0	5645
15	0.1230	0.950	25.8	4.65	-13.42	4.68	5.0	55.0	5575
16	0.1310	0.299	24.9	4.88	-1.39	2.92	5.0	60.0	6252
17	0.1320	0.349	23.9	6.26	-3.21	4.86	5.0	64.0	6282
18	0.1240	0.361	23.2	6.25	-3.49	7.19	5.5	69.5	6584
19	0.1260	0.306	21.3	6.97	-3.31	7.96	5.0	74.5	6603
20	0.1350	0.326	22.9	5.21	-4.41	8.72	6.0	80.5	6663
21	0.1460	0.312	23.1	5.01	0.48	9.66	5.5	86.0	6903
22	0.1670	0.498	20.9	5.31	1.75	9.92	7.5	93.5	7014
23	0.1390	0.498	20.2	6.99	3.04	9.71	7.0	100.5	7654
24	0.1500	0.489	20,0	6.30	-6.20	11.24	7.5	108.0	7684

25	0.1670	0.487	20.9	6.05	16.75	12.89	8.5	116.5	7719
26	0.1650	0.577	20,3	7.26	5.16	11.08	8.5	125.0	7789
27	0.2080	0.495	20.8	5.19	17.87	8.95	9.5	134.5	7820
28	0.1250	0.326	28.1	5.95	15.18	12.27	5.5	140.0	7860
29	0.1550	0.337	28.4	6.21	15.28	13.27	4.0	144.0	7884
30	0.1090	0.372	28.8	6.86	-19.98	17.31	3.5	147.5	7908

Before making a more detailed presentation of what Figures 6.13 – 6.17 and Table 6.10 show, we can state that we have here a good coverage of the experimental data from those produced by the developed and calibrated model. We want to highlight from the model calibration, and even motivated there, that for a coefficient in Equation (21) a dependence on the relative humidity of the air and its temperature is expected. We find this dependence in Table 6.10, which shows that at high relative humidity and temperature above 27 °C a is high (tests 1, 2, 26, 30) and that at low relative air humidity and temperature around 24 °C a has the lowest values (tests 10, 13, 14, 21, 27). Calculation of correlation coefficients of a vs. φ and a vs. $t_g/20$ finds the values 0.7551 and -0.2900, respectively, showing that a can, in the limit, be linearly related to φ and can be considered independent of t_g . Figure 6.18 supports these results. The line a vs. φ in this figure is given by Equation (32). Adding Equation (32) to Table 6.9, then all parameters of the evaporation-corrosion model are known.

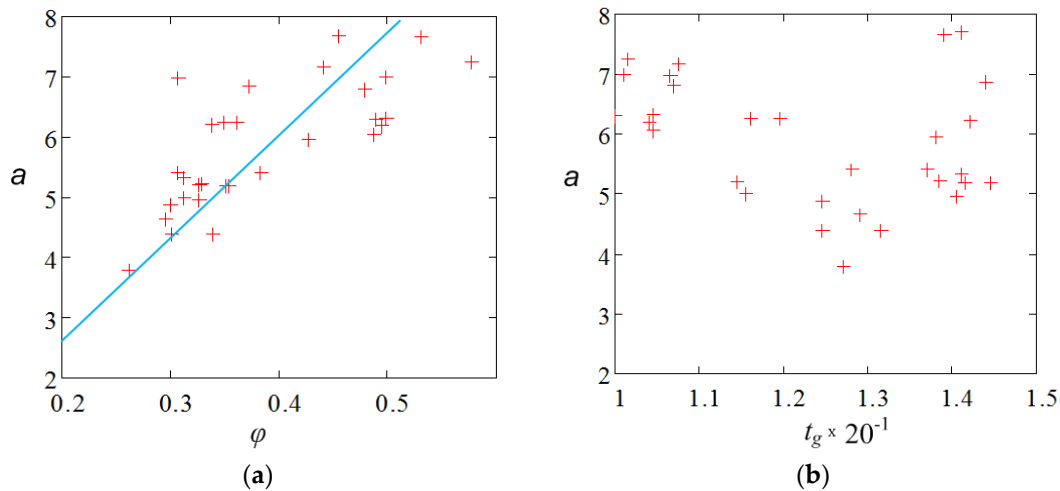


Figure 6.18. The evolution of a coefficient of Equation (21) in respect to the relative humidity of the air (a) and its temperature (b)

$$a = 2.423 + 8.839\varphi \quad (32)$$

The dynamics of the evaporation of a single droplet, having variable mass under variable environmental conditions (Table 6.10), is described well, even very well, by the developed model, as shown by the values of relative deviations experiment - model (Table 10, column ε_{mpM}) together with graphical representations from Figures 6.13-6.15.

Considering the model curve and the experimental curve for each evaporation test (Figures 6.13-6.15), we note their good correspondence, which supports the quality of the model. From 30 sets of curves, only in the case of test 27 and maybe test 25 does it appear that the model-experiment agreement is borderline. Figures 6.13-6.15, as well as Figures 6.16-6.17, in conjunction with the data in Table 6.10, show that the evaporation time of the drop depends on its size and the relative humidity and temperature of the air. The plots in Figures 6.17 and Figure 6.18(b), showing the dynamics of the rust mass from each of the 30 experiments, were drawn using the data provided by the model. The slope of these lines, which represent the corrosion rate, is almost the same for tests 1-27 where the water droplet contained no added ions. The nearly three-fold increase in this slope when we have 1g/L $NaCl$ in the droplet (tests 28, 29 and 30) shows the intensification of the corrosion rate by suppressing the cathodic reactions in the corrosion pile. The representation in Figure 6.18, right side, shows the very good agreement between the dynamics of the rust mass deposited under the drop, obtained experimentally and by

modeling. Thus, the approach of modeling the corrosion process through a droplet oxygen transfer model with chemical reaction on the steel surface is very well supported. Here too we can observe the above-mentioned change in the evolution of the slope when the composition of the droplet is changed by the addition of ions.

In subchapter 6.3.6. *Conclusions*, it was shown that the expression, in the evaporation-corrosion model of the evaporation surface of the momentary mass characteristic of the droplet, was solved by integral mathematical analysis in relation to the proven shape of the droplet. It has been shown that the evaporation of the droplet occurs with the preservation of the original shape and that the rust resulting from corrosion is deposited on this shape. For all 30 evaporation-corrosion tests, a very good coverage of the experimental results of droplet evaporation dynamics was obtained.

Excellent model-experiment agreement was obtained regarding the dynamics of the rust mass associated with a droplet.

In the case of evaporation - droplet corrosion with *NaCl* content, the involvement of *Cl* ions in the anodic corrosion process, led to a strong change in the reaction rate constant and the oxygen diffusion coefficient through the rust layer values, so that to obtain, for the dynamics of the mass deposited by the rust, a good agreement between the model and the experiment.

Selective references:

1. Castillo, J.E.; Weibel, J.A.; Garimella, S.V. The Effect of Relative Humidity on Dropwise Condensation Dynamics. *International Journal of Heat and Mass Transfer*, CTRC, **2014**, <https://doi.org/10.1016/j.ijheatmasstransfer.2014.09.080>.
2. Parekh, S.; Farid, M.M.; Selman, J.R.; Al-Hallaj S. Solar desalination with a humidification-dehumidification technique: A comprehensive technical review. *Desalination*, **2004**, 160, 167–186.
3. Dobre, T.; Stoica, A. *Mass Transfer Intensification*, Chapter 7, Electra Publishing House, 2017.
4. Ahmed, S.; Hou, Y.; Lepkova, K.; Pojtanabuntoeng T. Investigation of the effect chloride ions on carbon steel in closed environments at different temperatures. *Corros. Mater. Degrad.* **2023**, 4, 364–381.
5. Morcillo, M.; Chico B.; Alcantara J.; Diaz I.; Simancas J.; De la Fuente D. Atmospheric corrosion of mild steel in chloride-rich environments. Questions to be answered. *Materials and Corrosion*, **2015**, 66, 882-892.

ANNEXES - Supplemental materials for observing the corrosion process in the droplet

ANEXA I –Experimental data by days

Data Recepi i exp	Diam m mm	Numar m m	Temp m m	Alaza m m	Masa m m	Masa m m	Varian m m	Diam m m	Diam m m	Rust m m	Data m m	Data m m	Time m m
Data m m	Diam m m	Numar m m	Temp m m	Alaza m m	Masa m m	Masa m m	Varian m m	Diam m m	Diam m m	Rust m m	Data m m	Data m m	Time m m
07.07.2 Exp. 1	1	0	482.15	485.85	0.00								
	2	30	482.40	485.85	0.00								
	3	60	482.80	485.85	0.00								
	4	90	482.45	485.85	0.00								
	5	120	482.30	485.85	0.00								
	6	150	482.30	485.85	0.00								
	7	180	482.30	485.85	0.00								

(a) Exp. 1-2

Data Recepi i exp	Diam m mm	Numar m m	Temp m m	Alaza m m	Masa m m	Masa m m	Varian m m	Diam m m	Diam m m	Rust m m	Data m m	Data m m	Time m m
Data m m	Diam m m	Numar m m	Temp m m	Alaza m m	Masa m m	Masa m m	Varian m m	Diam m m	Diam m m	Rust m m	Data m m	Data m m	Time m m
09.07.2 Exp. 3	1	0	482.15	485.85	0.00								
	2	30	482.40	485.85	0.00								
	3	60	482.80	485.85	0.00								
	4	90	482.45	485.85	0.00								
	5	120	482.30	485.85	0.00								
	6	150	482.30	485.85	0.00								
	7	180	482.30	485.85	0.00								

(b) Exp 3-5

Data Recepi i exp	Diam m mm	Numar m m	Temp m m	Alaza m m	Masa m m	Masa m m	Varian m m	Diam m m	Diam m m	Rust m m	Data m m	Data m m	Time m m
Data m m	Diam m m	Numar m m	Temp m m	Alaza m m	Masa m m	Masa m m	Varian m m	Diam m m	Diam m m	Rust m m	Data m m	Data m m	Time m m
13.07.2 Exp. 6	1	0	482.40	487.20	0.00								
	2	30	485.85	1.55									
	3	60	483.70	1.95									
	4	90	482.80	0.70									
	5	120	482.45	0.55									
	6	150	482.45	0.00									
	7	180	482.45	0.00									

(c) Exp 6-8

Data Recepi i exp	Diam m mm	Numar m m	Temp m m	Alaza m m	Masa m m	Masa m m	Varian m m	Diam m m	Diam m m	Rust m m	Data m m	Data m m	Time m m
Data m m	Diam m m	Numar m m	Temp m m	Alaza m m	Masa m m	Masa m m	Varian m m	Diam m m	Diam m m	Rust m m	Data m m	Data m m	Time m m
13.07.2 Exp. 7	1	0	482.45	487.80	0.00								
	2	30	486.00	1.75									
	3	60	484.70	1.35									
	4	90	483.15	1.55									
	5	120	482.55	0.60									
	6	150	482.55	0.00									
	7	180	482.55	0.00									

(d) Exp 9-11

Data Recepi i exp	Diam m mm	Numar m m	Temp m m	Alaza m m	Masa m m	Masa m m	Varian m m	Diam m m	Diam m m	Rust m m	Data m m	Data m m	Time m m
Data m m	Diam m m	Numar m m	Temp m m	Alaza m m	Masa m m	Masa m m	Varian m m	Diam m m	Diam m m	Rust m m	Data m m	Data m m	Time m m
14.07.2 Exp. 9	1	0	482.60	486.90	0.00								
	2	30	487.70	1.30									
	3	60	486.45	1.85									
	4	90	485.30	1.15									
	5	120	484.10	1.00									
	6	150	483.15	0.95									
	7	180	482.75	0.40									
	8	210	482.75	0.00									
	9	240	482.75	0.00									
	10	270	482.75	0.00									
	11	300	482.75	0.00									

Exp. 13	1	0	481.02	492.00	0.00	24.3	32.0	6.0	22.8	83.0	1.0	78.0	5512.0
2	800	491.85	1.45			24.8	30.8	8.3					5513.8
3	1300	489.78	3.52			24.2	30.2	9.0					5515.6
4	1800	487.71	5.59			24.6	29.9	9.3					5517.4
5	2300	485.64	7.66			24.9	29.5	9.9					5519.2
6	2800	483.57	9.73			24.7	33.1	8.7					5521.0
7	3300	481.50	11.80			24.8	30.2	9.1					5522.8
8	3800	479.43	13.87			24.8	30.2	9.1					5524.6
9	4300	477.36	15.94			24.8	30.2	9.1					5526.4
10	4800	475.29	18.01			24.8	30.2	9.1					5528.2
11	5300	473.22	20.08			24.8	30.2	9.1					5530.0
12	5800	471.15	22.15			25.1	28.9	8.1					5531.8
13	6300	469.08	24.22			25.3	25.4	4.1					5533.6
14	6800	467.01	26.29			25.8	26.1	6.7					5535.4
15	7300	464.94	28.36			25.7	24.8	4.0					5537.2
16	7800	462.87	30.43			25.6	25.0	4.5					5539.0
17	8300	460.80	32.50			25.6	26.5	4.8					5540.8
18	8800	458.73	34.57			25.3	18.4	4.7					5542.6
19	9300	456.66	36.64			25.1	22.0	3.9					5544.4
20	9800	454.59	38.71			25.2	22.0	3.9					5546.2
21	10300	452.52	40.78			25.2	22.0	3.9					5548.0
22	10800	450.45	42.85			25.2	22.0	3.9					5549.8
23	11300	448.38	44.92			25.2	22.0	3.9					5551.6
24	11800	446.31	46.99			25.2	22.0	3.9					5553.4
25	12300	444.24	49.06			25.2	22.0	3.9					5555.2
26	12800	442.17	51.13			25.2	22.0	3.9					5557.0
27	13300	440.10	53.20			25.2	22.0	3.9					5558.8
28	13800	438.03	55.27			25.2	22.0	3.9					5560.6
29	14300	435.96	57.34			25.2	22.0	3.9					5562.4
30	14800	433.89	59.41			25.2	22.0	3.9					5564.2
31	15300	431.82	61.48			25.2	22.0	3.9					5566.0
32	15800	429.75	63.55			25.2	22.0	3.9					5567.8
33	16300	427.68	65.62			25.2	22.0	3.9					5569.6
34	16800	425.61	67.69			25.2	22.0	3.9					5571.4
35	17300	423.54	69.76			25.2	22.0	3.9					5573.2
36	17800	421.47	71.83			25.2	22.0	3.9					5575.0
37	18300	419.40	73.90			25.2	22.0	3.9					5576.8
38	18800	417.33	75.97			25.2	22.0	3.9					5578.6
39	19300	415.26	78.04			25.2	22.0	3.9					5580.4
40	19800	413.19	80.11			25.2	22.0	3.9					5582.2
41	20300	411.12	82.18			25.2	22.0	3.9					5584.0
42	20800	409.05	84.25			25.2	22.0	3.9					5585.8
43	21300	406.98	86.32			25.2	22.0	3.9					5587.6
44	21800	404.91	88.39			25.2	22.0	3.9					5589.4
45	22300	402.84	90.46			25.2	22.0	3.9					5591.2
46	22800	400.77	92.53			25.2	22.0	3.9					5593.0
47	23300	398.70	94.60			25.2	22.0	3.9					5594.8
48	23800	396.63	96.67			25.2	22.0	3.9					5596.6
49	24300	394.56	98.74			25.2	22.0	3.9					5598.4
50	24800	392.49	100.81			25.2	22.0	3.9					5599.2

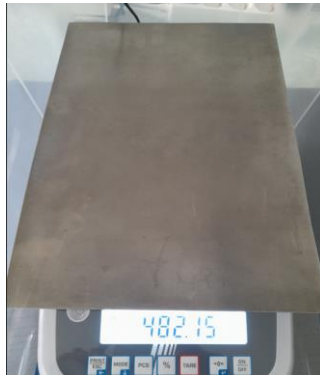
(e) Exp 13-15

Exp. 17	1	0	481.02	492.00	0.00	24.3	32.0	6.0	22.8	83.0	1.0	78.0	5512.0
2	800	491.85	1.45			24.8	34.2	7.0					5513.8
3	1300	489.78	3.52			23.8	36.2	7.0	22.0	68.0	1.0	78.0	5515.6
4	1800	487.71	5.59			23.8	35.1	7.4					5517.4
5	2300	485.64	7.66			24.0	34.2	7.2					5519.2
6	2800	483.57	9.73			24.0	34.2	7.2					5521.0
7	3300	481.50	11.80			24.0	34.2	7.2					5522.8
8	3800	479.43	13.87			24.0	34.2	7.2					5524.6
9	4300	477.36	15.94			24.0	34.2	7.2					5526.4
10	4800	475.29	18.01			24.0	34.2	7.2					5528.2
11	5300	473.22	20.08			24.0	34.2	7.2					5530.0
12	5800	471.15	22.15			24.0	34.2	7.2					5531.8
13	6300	469.08	24.22			24.0	34.2	7.2					5533.6
14	6800	467.01	26.29			24.0	34.2	7.2					5535.4
15	7300	464.94	28.36			24.0	34.2	7.2					5537.2
16	7800	462.87	30.43			24.0	34.2	7.2					5539.0
17	8300	460.80	32.50			24.0	34.2	7.2					5540.8
18	8800	458.73	34.57			24.0	34.2	7.2					5542.6
19	9300	456.66	36.64			24.0	34.2	7.2					5544.4
20	9800	454.59	38.71			24.0	34.2	7.2					5546.2
21	10300	452.52	40.78			24.0	34.2	7.2					5548.0
22	10800	450.45	42.85			24.0	34.2	7.2					5549.8
23	11300	448.38	44.92			24.0	34.2	7.2					5551.6
24	11800	446.31	46.99			24.0	34.2	7.2					5553.4
25	12300	444.24	49.06			24.0	34.2	7.2					5555.2
26	12800	442.17	51.13			24.0	34.2	7.2					5557.0
27	13300	440.10	53.20			24.0	34.2	7.2					5558.8
28	13800	438.03	55.27			24.0	34.2	7.2					5560.6
29	14300	435.96	57.34			24.0	34.2	7.2					5562.4
30	14800	433.89	59.41			24.0	34.2	7.2					5564.2
31	15300	431.82	61.48			24.0	34.2	7.2					5566.0
32	15800	429.75	63.55			24.0	34.2	7.2					5567.8
33	16300	427.68	65.62			24.0	34.2	7.2					5569.6
34	16800	425.61	67.69			24.0	34.2	7.2					5571.4
35	17300	423.54	69.76			24.0	34.2	7.2					5573.2
36	17800	421.47	71.83			24.0	34.2	7.2					5575.0
37	18300	419.40	73.90			24.0	34.2	7.2					5576.8
38	18800	417.33	75.97			24.0	34.2	7.2					5578.6
39	19300	415.26	78.04			24.0	34.2	7.2					5580.4
40	19800	413.19	80.11			24.0	34.2	7.2					5582.2
41	20300	411.12	82.18			24.0	34.2	7.2					5584.0
42	20800	409.05	84.25			24.0	34.2	7.2					5585.8
43	21300	406.98	86.32			24.0	34.2	7.2					5587.6
44	21800	404.91	88.39			24.0	34.2	7.2					5589.4
45	22300	402.84	90.46			24.0	34.2	7.2					5591.2
46	22800	400.77	92.53			24.0	34.2	7.2					5593.0
47	23300	398.70	94.60			24.0	34.2	7.2					5594.8
48	23800	396.63	96.67			24.0	34.2	7.2					5596.6
49	24300	394.56	98.74			24.0	34.2	7.2					5598.4
50	24800	392.49	100.81			24.0	34.2	7.2					5599.2

(f) Exp 17-19

Exp. 22	1	0	481.02	492.00	0.00	24.3	32.0	6.0	22.8	83.0	1.0	78.0	5512.0
2	800	491.85	1.45			24.1	42.0	7.6					5513.8
3	1300	489.78	3.52			21.2	42.4	7.9	15.0	67.0	6.0	78.0	5515.6
4	1800	487.71	5.59			21.2	42.3	7.8					5517.4
5	2300	485.64	7.66			21.2	42.3	7.8					5519.2
6	2800	483.57	9.73			21.2	42.3	7.8					5521.0
7	3300	481.50	11.80			20.9	44.0	8.2					5522.8
8	3800	479.43	13.87			20.7	44.2	8.1					5524.6
9	4300	477.36	15.94			20.6	44.9	8.2					5526.4
10	4800	475.29	18.01			20.7	44.3	8.1					5528.2
11	5300	473.22	20.08			20.7	44.4	8.1					5530.0
12	5800	471.15	22.15			20.7	44.4	8.1					5531.8
13	6300	469.08	24.22			20.5	45.9	8.4					5533.6
14	6800	467.01	26.29			20.5	45.9	8.4					5535.4
15	7300	464.94	28.36			20.5	45.9	8.4					5537.2
16	7800	462.87	30.43			20.5	45.9	8.4					5539.0

ANEXA III – Corrosion dynamics from droplet initiation to corrosion acceleration experiments



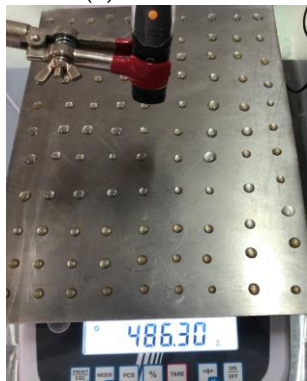
(a) 7 iul 2022



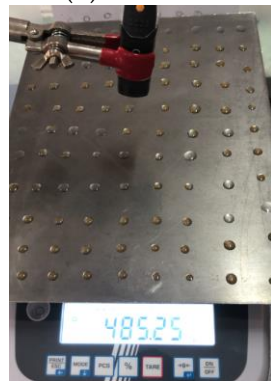
(b) 7 Iul 2022



(c) 7 Iul 2022



(a) SEP 2022



(b) Mar 202



(c) Apr 2023



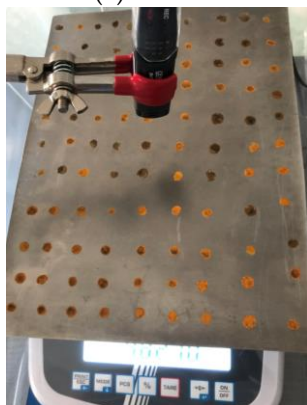
(a) iul 2022



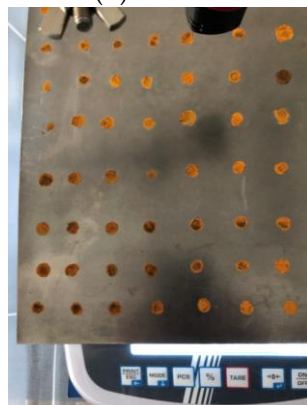
(b) iul 2022



(c) Iul 2022 (2)



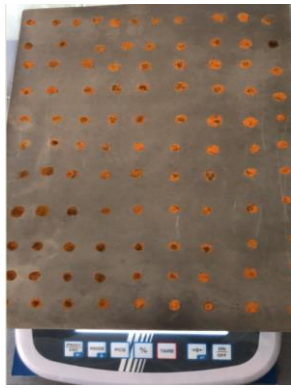
(a) iul 2022



(b) iul 202



(c) iul 2023



(a) iul 2022



(b) iul 2022



(c) sep 2022



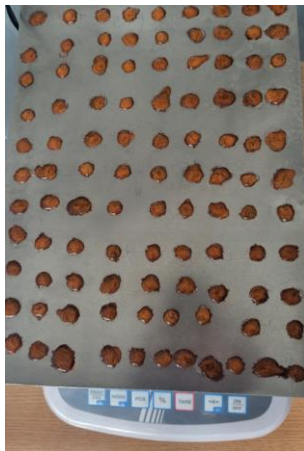
(a) oct 2023



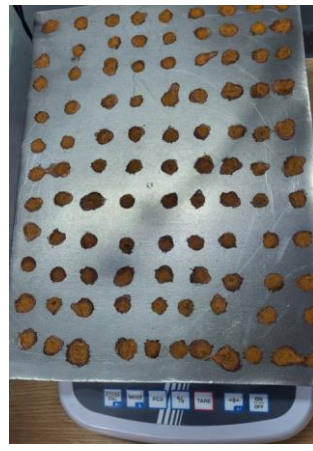
(b) nov 2022



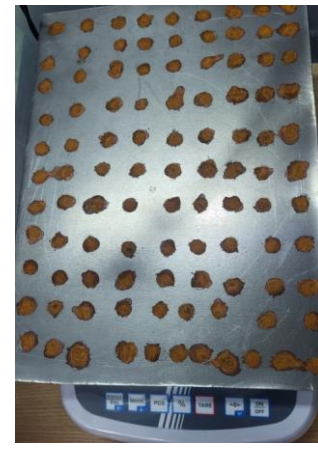
(c) feb 2023



(a) Mar 2022



(b) Iul 2022



(c) Iul 2022 (2)



(a) april 2023



(b) april 2023



(c) mai 2023



(a) iul 2023



(b) iul 2023



(c) iul 2023

4. Conclusions of thesis

The general conclusions were kept in the format of the thesis

The research *Mass transfer to the corrosion of oil terminals* started from the assessment that oil terminals must be high safety installations in operation, so they must be protected, first of all, from the deterioration due to corrosion, specifically from the deterioration due to atmospheric corrosion. Protection from the risk of corrosion is done through a deeper knowledge of it and in this sense it has been appreciated that this can be done by analyzing the transport and transfer to the corrosion surface of the species that intervene in its attack reaction. More precisely, the dynamics of the corrosion process was considered to be based on the transport and transfer through the corrosion medium towards the surface reaction of the main active species (oxygen in pure corrosion). It was then found that the transport and transfer through the corrosion medium can exist, being more complicated in fact as the simultaneous transport and transfer of mass and heat (the case of droplet corrosion). Based on these considerations, the structure of the research was built, and the particularities of experimental investigation and modeling were developed. Thus, a work with personality and originality was achieved.

As is customary in the chapter of general conclusions, there is actually a review of what the thesis brings new, interesting and original. In fact, each of the previous chapters of the thesis has its own imprint and elements, which are listed in the chapter conclusions. In the spirit of this consideration, we specify the following.

1. One of the objectives proposed for this research was the familiarization with the multiple processes and characteristic phenomena in the field of corrosion, through an intensive study of the specific literature, and this objective is considered, through the prism of the first two chapters of the study, as well as through the introductory sub-chapters addressed at all the chapters in this work, achieved.

2. It was shown that the similarity between corrosion, pickling and etching of metal surfaces allows to approach them through the same type of models of species transfer and chemical reaction on the surface. In particular, mathematical models for metal pickling by immersion and by spraying techniques can be developed by simultaneously solving the equations of flow and diffusion of species towards the active surface. It was thus possible to develop a mathematical model to describe the pickling dynamics. The obtained model was in agreement, within normal limits, with the experimental data when it was customized for copper pickling with ammonium persulfate and sulfuric acid solutions. The concentrated model in the solute flux relation $N_p = c \left(\frac{D^3}{\nu H} \right)^{0.25} c_{pa}^{1.25}$ is general and can be used in the calculation of pickling baths for any metal species.

3. We demonstrated with the theoretical part that corrosion is a surface chemical phenomenon, so we took the research to this level, with the study and experimental investigation on two fundamental directions in atmospheric corrosion, namely film corrosion and droplet corrosion.

4. Thus, two laboratory installations were built to investigate each phenomenon separately and their associated operating procedures were elaborated, so that the surface corrosion dynamics of steel could be characterized when the surface corrosive medium is in film, film flow or droplets.

5. A complex mathematical model with partial differential equations and ordinary differential equations for O_2 , Fe^{2+} și $Fe(OH)_3$, was considered for the analysis of the experimental data in the film flow corrosion, and the numerical transposition of the model allowed the identification of the model parameters, in particular of the apparent surface corrosion rate constant and the surface oxidation yield of Fe^{2+} from corrosion. It was observed that the oxidation yield of iron ions on the surface of the rust film is not influenced by the intensity of the surface film flow and the age of the rust deposit. Considering the identified dynamics of the oxygen diffusion coefficient through the rust deposit, it was found that over time the surface rust deposit becomes increasingly resistant to oxygen diffusion, for which two distinct domains were identified.

6. A complex mathematical model based on simultaneous heat and mass transfer and simultaneous oxygen transfer with surface reaction was considered to analyze the experimental droplet evaporation-corrosion data. The expression in the evaporation-corrosion model of the evaporation surface and oxygen transfer as a function of the moment mass of the droplet was solved by integral mathematical analysis in relation to the accepted shape of the droplet. It has been shown that the evaporation of the drop occurs with the preservation of the original trace and that the rust resulting from corrosion is deposited on this trace. The numerical transposition of the model allowed obtaining the values and strategies for certain parameters of the model specifying here the surface reaction speed constant (k_{rs}), and the effective oxygen diffusion coefficient through the rust layer (D_{O2ef}). For all evaporation-corrosion tests, a good agreement of the experimental results of droplet evaporation dynamics was obtained. Excellent model-experiment agreement was obtained regarding the dynamics of the rust mass associated with a droplet. In the case of evaporation corrosion in drops containing $NaCl$, the involvement of Cl ions in the anodic corrosion process led to a strong change in the reaction rate constant and the oxygen diffusion coefficient through the rust layer values, so that in this case, for the dynamics of the deposited rust mass, a good agreement between the model and the experiment was obtained.

Aknowledgement:

This work has been funded by the European Social Fund from the Sectoral Operational Programme Human Capital 2014-2020, through the Financial Agreement with the title “Training of PhD students and postdoctoral researchers in order to acquire applied research skills—SMART”, Contract no. 13530/16.06.2022—SMIS code: 153734.